Influence of El Niño on atmospheric CO_2 over the tropical Pacific Ocean: findings from NASA's OCO-2 mission

A. Chatterjee[1,2*], M. M. Gierach[3], A. J. Sutton[4,5], R. A. Feely[4], D. Crisp[3], A. Eldering[3], M. R. Gunson[3], C. W. O'Dell[6], B. B. Stephens[7], D. S. Schimel[3]

[1] Universities Space Research Association, Columbia, MD

[2] NASA Global Modeling and Assimilation Office, Greenbelt, MD

[3] Jet Propulsion Laboratory, California Institute of Technology, Pasadena, CA

[4] NOAA Pacific Marine Environmental Laboratory, Seattle, WA

[5] Joint Institute for the Study of the Atmosphere and Ocean, University of Washington, Seattle, WA

[6] Colorado State University, Fort Collins, CO

[7] National Center for Atmospheric Research, Boulder, CO

*Correspondence to: abhishek.chatterjee@nasa.gov

Abstract:

Space-borne observations of CO_2 from the Orbiting Carbon Observatory-2 are used to characterize the response of the tropical atmospheric CO_2 concentrations to the strong El Niño event of 2015-2016. Correlations between atmospheric CO_2 growth rate and the El Niño Southern Oscillation have been well known; however, the magnitude of the correlation and the timing of the responses of oceanic and terrestrial carbon cycle remain poorly constrained in space and time. Here we use space-based CO_2 observations to confirm that the tropical Pacific Ocean does play an early and important role in modulating the changes in atmospheric CO_2 concentrations during El Niño events – phenomenon inferred but not previously observed due to lack of high-density, broad-scale CO_2 observations over the Tropics.

One Sentence Summary:

NASA's OCO-2 mission provides a first-hand look at the space-time evolution of tropical atmospheric CO_2 concentrations in response to the 2015-2016 El Niño

Main Text:

El Niño Southern Oscillation, or ENSO, is the dominant mode of tropical climate variability on interannual to decadal timescales (*1-5*) and is correlated with large inter-annual variability in global atmospheric CO_2 concentrations (*6-19*). Studying the response of the carbon cycle to this natural climate phenomenon is critical to understand and quantify the sensitivity of the carbon cycle to climate variability, and by extension to climate generally (*20*). Although the ENSO cycle originates in the equatorial Pacific, its impact on the carbon cycle is felt globally due to its regional teleconnections (*22-23*) and influences on atmospheric and ocean circulation, precipitation, temperature, and fire emissions (*1, 24-26*). Partitioning the response of the constituent components of the carbon cycle to a complete El Niño event has been challenging because of the limited number of CO_2 observations over the tropical land and ocean regions.

Observations of atmospheric CO_2 from space provide a global view of the carbon cycle that can be used to describe phenomena that have been previously pieced together from sparse *in situ* data. NASA's Orbiting Carbon Observatory-2 (OCO-2) mission was successfully launched on July 2, 2014 and started providing science data in early September 2014 (*70*). Within the first two years of operation of the OCO-2 mission, a major El Niño (warm phase of the ENSO) occurred (*27-30*). We provide an approach for studying the temporal sequence of El Niño-induced changes in global CO_2 concentrations using observations from the OCO-2 mission that are validated with the Tropical Atmosphere Ocean (TAO) mooring CO_2 data. We see a response from the tropical Pacific Ocean during the early stages of an El Niño event and a lagged (and much larger) terrestrial signal as the El Niño reaches maturity.

El Niño and the global carbon cycle

Correlations between the atmospheric CO_2 growth rate and El Niño activity have been reported since the 1970s (*6-8*, *31-32*), although the magnitude and timing of the responses of the ocean and terrestrial components remain poorly constrained (*33*). Here, the word terrestrial includes both changes in biospheric productivity (respiration and photosynthesis) as well as biomass burning (fires). Following previous strong El Niño events (for example, the 1982-1983 and 1997-1998 El Niño events), methods for measuring the atmospheric CO_2 response to ENSO were based on *in situ* atmospheric CO_2 observations at a handful of surface stations that transect the tropical Pacific, including Mauna Loa, Christmas Island and American Samoa (*8*, *34*) as well as shipboard transect measurements (*12*, *35-36*). The annual growth rate of atmospheric CO_2 measured at these remote stations and other sites around the globe show remarkable correlation with ENSO indices, with a rapid increase in atmospheric CO_2 associated with the late stage of an El Niño event (*19*, *37*). The ocean response to El Niño events is based on studies looking at *in situ* observations, for example, surface ocean pCO_2 observations from ships of opportunity (*12*), moorings (*38-39*), or targeted field campaigns during El Niño events (*9-10*, *40-41*), and a variety of mechanistic ocean models (*24*, *52*, *54*, *61, 65, 67*).

The overall increase in the release of CO_2 to the atmosphere during strong El Niño events has been attributed to a decrease in biospheric uptake of CO_2 (e.g., due to drying of tropical land regions and an increase in plant and soil respiration) combined with enhanced fire emissions. In recent years, this has led to a growing body of literature (*42-49*) concluding that ENSO-mediated variability in tropical net land primary productivity is what primarily influences the atmospheric CO_2 growth rate. A handful of studies (*25*, *50-51*) have disputed any consistent or coherent response from the land component during El Niño events, thus highlighting the high level of uncertainty and disagreement within the carbon cycle community.

The El Niño-CO_2 signature should have a significant tropical Pacific Ocean component as well, with opposite sign to the terrestrial response (*10*, *13*, *33*). During strong El Niño events, there is a large-scale weakening of the easterly trade winds and suppression of eastern equatorial Pacific upwelling (indicated by a deeper thermocline) that reduces the supply of cold, carbon-rich waters to the surface (Fig. 1). This reduces the usual strong outgassing of CO_2 from this region (*52-67*), typically on the order of ~0.4–0.6 PgC yr^{-1} to the atmosphere, by ~40-60% during an El Niño event (*9-12*, *33*, *36*, *60, 73*). If net fluxes were to remain constant elsewhere, these substantial net air-sea CO_2 anomalies should lead to a reduction in the growth rate of atmospheric CO_2, at least during the early stages of El Niño.

Understanding these variations in atmospheric CO_2, the timing of these variations and the underlying processes that cause them have been of great interest within the carbon cycle community (*1*, *10-13*, *15*, *20*, *33*, *50*). Integrating information from ocean- and atmosphere-based estimates, and modeling studies, we now know that it is the combined and opposite effect of ocean and terrestrial responses, which contribute to El Niño-related variations in atmospheric CO_2 (*33*). What remain controversial though are the timing of the ocean response and a precise quantification of its role. This is of crucial importance because typically the interannual variability (IAV) in the growth rate of atmospheric CO_2 is used to constrain the climate sensitivity of land carbon fluxes (γ_{LT}) (*20-21*); however, if a component of the IAV is being modified by ocean fluxes, then these inferences of γ_{LT} need to be reconsidered.

Because of the few surface CO_2 monitoring stations over the center of action (i.e., tropical Pacific Ocean), it has been challenging to directly observe the timing and changes in flux of CO_2 from the ocean to the atmosphere that affect the atmospheric CO_2 growth rate during an El Niño event. Efforts to analyze the data from distant measurement locations tend to identify the

enhanced CO_2 fluxes from the terrestrial carbon cycle, which dominate during the later stages of El Niño. The high-density, broad-scale observations of CO_2 from OCO-2 provide a valuable tool to partition the ocean and terrestrial carbon cycle responses to El Niño.

Time series of X_{CO2} anomalies during the 2015-2016 El Niño

OCO-2 observations describe the column-averaged CO_2 dry air mole fraction (X_{CO2}). More details regarding the OCO-2 mission, data features, X_{CO2} retrievals, etc. are provided in the Supplementary Materials, and are available in (*69*) and (*70*) while validation of X_{CO2} via comparisons to a ground-based network are provided in (*71*).

El Niño events are identified by warm sea surface temperature anomalies in precise regions of the tropical Pacific Ocean, with the most commonly used being the Niño 3.4 region (5°S-5°N, 170°W-120°W). Figs. 2A and 2B show the trend in X_{CO2} anomaly (*90*) for the Niño 3.4 region and its temporal evolution relative to two ENSO indices (*91*), including the Oceanic Niño Index (ONI - derived from sea surface temperature anomalies in the Niño 3.4 region) and the Southern Oscillation Index (SOI - derived from observed sea level pressure differences between Tahiti and Darwin, Australia). The 2015-2016 El Niño began around March 2015 and reached its peak over the Central Pacific between November 2015 and January 2016 (*30*). The X_{CO2} anomaly (Fig. 2B) shows two distinct periods over the entire El Niño event: (a) Development phase of El Niño (Spring-Summer 2015) – we argue that the negative X_{CO2} anomaly is due to a reduction in local CO_2 outgassing from the tropical Pacific Ocean, and (b) Mature phase of El Niño (Fall 2015 onwards) – we argue that the positive trend in X_{CO2} anomaly reflects an increase in atmospheric CO_2 concentrations due to terrestrial sources (i.e., combination of reduced vegetation uptake across pan-tropical regions and enhanced biomass burning emissions from SE Asia and Indonesia). The time series in Fig. 2B shows the space-

based CO_2 dataset documenting the response of the carbon cycle (both oceanic and terrestrial) during an entire El Niño event, capturing both the development and the mature phase and the transition between those two. The timing of the OCO-2 launch was extremely fortuitous in this regard.

Deriving the X_{CO2} anomalies require observations taken by both NASA's OCO-2 and the Japan Aerospace Exploration Agency's (JAXA) Greenhouse Gases Observing Satellite (GOSAT) (*68*) mission. The short OCO-2 record makes it impossible to fit a long-time series and calculate anomalies, and hence data from the GOSAT mission (operating since January 2009) was utilized to generate the X_{CO2} climatology. The OCO-2 team retrieved X_{CO2} from the first 7 years of the GOSAT observations using the same retrieval algorithm that generated the OCO-2 data product (*90*). Continuous global coverage from these two missions allows us to stitch together a long-time series of X_{CO2} over remote regions, such as the tropical Pacific Ocean (Figs. S1-S2). However, utilizing two data sources, i.e., GOSAT and OCO-2, can incur errors in the analyses due to changes in the two instruments, their observing strategies and sampling density. Fig. 2B also illustrates the corresponding uncertainty in our analyses. The uncertainty is calculated using an ensemble technique (Section C in Supplementary Materials) and further brings out the two phases in the time series of the Niño 3.4 X_{CO2} anomaly – ±0.3 ppm uncertainties during the El Niño development phase with both the upper and lower bounds below the zero line, and larger uncertainties of ±0.5 ppm during the mature phase of the El Niño event. These larger uncertainties during the latter stages of the El Niño illustrate the challenge in attributing the changes in X_{CO2} anomalies to the competing, and often opposing, signals from the ocean and the terrestrial components of the carbon cycle.

Attributing the two observed phases of X_{CO2} anomalies to the ocean and the terrestrial response

Our argument for the two observed phases in the X_{CO2} anomaly time series is supported by complementary data sources. The ocean response is corroborated by sea surface pCO_2 observations from an *in situ* network of autonomous CO_2 systems on the TAO moored buoy array (*9*, *38*, *72*). Data are not directly comparable to atmospheric X_{CO2} as they describe CO_2 variations at the ocean surface. The trend of the difference between the sea surface and atmospheric CO_2 (ΔpCO_2), however, does capture typical El Niño signatures. For example, Fig. 2C illustrates data from one of the moored buoys in the Niño 3.4 region (0°, 170°W), which shows decreasing ΔpCO_2 over the spring and near-zero ΔpCO_2 by December 2015. A suppression in the upwelling of CO_2-rich waters caused by weakening of the easterly trade winds leads to a reduction in the surface ocean carbon content, which in turn leads to a decline in the magnitude of sea-to-air CO_2 fluxes. The flux estimates at this buoy location are 1.35 ± 0.21 (1σ) gC m^{-2} $month^{-1}$ during the November 2014 to February 2015 period (i.e., non El Niño conditions) that gradually decrease to 0.087 ± 0.083 (1σ) gC m^{-2} $month^{-1}$ between November 2015 and February 2016 (i.e., El Niño conditions). This indicates a near-total shutdown of sea-to-air flux during Boreal Winter 2015-2016 relative to the neutral 2014-2015 Boreal Winter. Previous studies focusing on the tropical Pacific Ocean have reported flux reductions of ~40-60% over the entire basin (*9-12*, *33*, *36*, *60*, *73*). Atmospheric transport model calculations with a prescribed set of flux patterns and comparing to the observed X_{CO2} anomalies (Section A in Supplementary Materials) suggest a flux reduction of ~26-54%.

While these numbers are roughly similar, we do recognize the limitation in comparing flux estimates from one point (namely the TAO location at 0°, 170°W) to flux estimates for the

entire Niño 3.4 region and/or the tropical Pacific Ocean from previous studies. Large-scale changes in the physical and biogeochemical dynamics during El Niño events result in significant spatial and temporal variability in the surface pCO_2 distributions (*12*, *62*, *65*). Additionally, these spatial variations and their seasonal progression are uniquely tied to each El Niño event; thus, different flavors of El Niño events and/or shifts in the El Niño phenomena (*86-88*) will influence the evolution of the seasonal cycle of pCO_2 and air-sea CO_2 fluxes over the region. For the 2015-2016 El Niño event, the TAO buoy at 0°, 170°W lay closest to the edge of the warm pool and registered the first response to the onset of El Niño conditions. As observations from other TAO locations (*92*) are becoming available, it is evident that in the eastern part of the basin there was an overall suppression of the outgassing CO_2 source but with large variability in pCO_2. Data synthesis and modeling work with these and other *in situ* observations are ongoing to quantify the exact magnitude of ocean CO_2 fluxes over different tropical Pacific regions during the 2015-2016 El Niño.

The second phase in the X_{CO2} anomaly time series is driven by the terrestrial component of the carbon cycle, and the transport of this signal to the remote Niño 3.4 region. The anomalous increase in CO_2 can be attributed to a combination of terrestrial sources, including a reduction in the global biospheric uptake, increases in soil and plant respiration and enhanced fire emissions. In fact, the impact of enhanced fire emissions and their regional progression was a well-studied feature following the strong 1997-1998 El Niño (*26*, *43*, *74-76*). For the 2015-2016 El Niño event, strong correspondences between X_{CO2} from OCO-2 and the carbon monoxide (CO) total column anomalies from the Measurements of Pollution in the Troposphere (MOPITT) instrument on the NASA Terra platform, are evident over the tropical Pacific Ocean, especially during Fall 2015 (Fig. 2D). We conjecture that these CO total column anomalies are

representative of the emissions from the 2015–2016 Indonesian peat fires (*77-80*), which were advected into the tropical Pacific region. El Niño-related changes in the Walker circulation (i.e., westerly winds) and the slightly more southern than normal positioning of the Inter Tropical Convergence Zone (ITCZ) (*81*) may allow emissions from the Indonesian peat fires to carry over into this region (Fig. S4). It is interesting to note from Figs. 2B and 2D that the positive increase in X_{CO2} anomaly actually leads the fire signals by 1-2 months. This indicates that the release of carbon flux resulting in an increase in CO_2 concentrations is only partially pyrogenic; reduced vegetation uptake due to droughts is a significant contributor, and quite possibly the initial cause of the increase in X_{CO2} anomaly.

Isolating the observed negative X_{CO2} anomaly to an ocean signal

The time dependence of the X_{CO2} anomalies during the 2015-2016 El Niño indicate that the initial decrease in atmospheric CO_2 is due to suppression of upwelling in the tropical Pacific. This early negative response is subsequently offset by a large positive anomaly due to the terrestrial component. Assuming no significant interannual changes elsewhere in the global ocean, we can further confirm our argument by a comparison of the X_{CO2} anomaly in the Niño 3.4 region with the global X_{CO2} anomaly (Fig. 4A). By differencing the far-field effect from the local signal, the influence of the reduction in CO_2 outgassing from the tropical Pacific Ocean is clearly visible during the onset phase of El Niño. The peak reduction registered over the Niño 3.4 region relative to the global X_{CO2} anomalies is 0.35 ppm in June 2015, which occurs a couple of months after the initiation of the El Niño event. Lag correlation of the Niño 3.4 X_{CO2} anomalies against the ONI index indicate that the highest positive correlation occurs when the concentration-related anomalies lag the SST-related anomalies by 1-2 months (*93*) (Fig. S8). The time lag relationship can be precisely quantified during the onset phase of El Niño, but it is much

more difficult to interpret during the succeeding El Niño stages when any reduction in CO_2 from decreased equatorial upwelling is masked by the signal from terrestrial processes. Thus, if it were not for the reduction in outgassing from the ocean, the impact from the terrestrial sources would likely be larger. Our analysis confirms the findings from (*13*) that the slowdown of atmospheric CO_2 increase during the early stages of an El Niño is indeed related to the decreased sea-to-air flux of CO_2 in the tropical Pacific Ocean. The coverage from the OCO-2 mission has enabled us to verify this hypothesis and monitor its temporal evolution using real atmospheric CO_2 observations.

The early stage negative X_{CO2} anomaly is unique to the tropical Pacific Ocean and is not influenced by global, terrestrial or large-spatial scale fluxes. Due to the large interhemispheric gradients in CO_2, typical variability in tropical CO_2 concentrations can be an aliasing of terrestrial processes occurring at higher latitudes. In order to confirm that the recovered ocean signal in the X_{CO2} anomaly is unique to the tropical Pacific Ocean, we examined three other ocean regions - the subtropical North Pacific (20°-30°N, 120°-170°W), the subtropical South Pacific (20°-30°S, 120°-170°W) and the tropical Atlantic Ocean (5°N -5°S, 5°-35°W). Fig. 3 shows the specific regions (aside from Niño 3.4) that we have analyzed, and each of which assist us to reject alternative hypotheses. Non-zero differences in X_{CO2} anomalies between these and the Niño 3.4 region (Fig. 4) indicate that the trend observed over the tropical Pacific Ocean is distinct from other ocean basins. This makes intuitive sense from our mechanistic understanding as well - while large impacts of ENSO on the sea-to-air CO_2 flux in the tropical Pacific Ocean are expected, studies have shown minute and delayed influence of the ENSO modes on the variability of carbon fields in the tropical Atlantic Ocean (*66*, *82-83*).

Perspective

The strong El Niño in 2015-2016 caused a reduction in the magnitude of CO_2 outgassing from the tropical Pacific Ocean. These changes, albeit of varying magnitude, extended over a large portion of the tropical Pacific, and impacted the large-scale modulation of the physical processes responsible for the CO_2 efflux from this region. Almost all observing networks (i.e., OCO-2, TAO, etc.) were aided by the strength of this signal. However, OCO-2 provided a more comprehensive view of the tropical Pacific Ocean signal than previous observing networks given its: (a) greater coverage and more frequent sampling than *in situ* networks, and (b) improved resolution and precision than earlier space-based instruments. For example, GOSAT, like OCO-2 is sensitive to the total CO_2 column, but has lower precision (2 ppm single sounding random error for GOSAT vs. 0.5 ppm for OCO-2) and lower sampling density (100x less soundings). The immediate next step will be to fold in these observations into an inverse modeling framework (*13*, *15, 50, 56*) to infer the underlying net fluxes between the ocean and atmosphere and the terrestrial biosphere and the atmosphere. This would help establish the real benefit of OCO-2, especially against the backdrop of previous studies that had to rely on sparse atmospheric constraint to infer changes in CO_2 surface fluxes during El Niño events.

Based on OCO-2 data alone, however, we cannot quantitatively discriminate the relative roles of reduction in biospheric activity uptake due to a warmer and drier climate in 2015 versus enhanced fire emissions. While we can quantify the temporal response of the ocean versus the terrestrial component and qualitatively observe the gradients in the response of different tropical Pacific Ocean regions (Fig. 5), it is much more challenging to discriminate the contribution of fire emissions and the delayed response of the terrestrial biosphere to El Niño-induced changes in weather patterns. The impact of ENSO is typically felt by the terrestrial biosphere over several months to a year after the actual event. Studies on both progressions of droughts (*84*) and fires

(*26*) during an El Niño cycle have shown a hysteresis in the Earth system's response to changes in temperature and precipitation patterns. Analyses using ancillary data sources such as solar-induced fluorescence (SIF), bottom-up model simulations and inverse modeling calculations are typically necessary to quantify the partitioning of the terrestrial carbon fluxes (reduction in biospheric uptake vs. increase in fire emissions) as has been pursued in a companion study (*85*).

Our study provides a short-term perspective on the potential of CO_2 observations from space for unraveling more complex relationships of carbon sources and sinks in the future. A longer time series of observations will enable testing more hypotheses such as the possibility of regionally dependent gradients in air-sea CO_2 fluxes in the tropical Pacific, or adding data to support biogeochemical theories at previously inaccessible scales. From a long-term perspective, such information will improve our process-based understanding, inform our current suite of mechanistic models, and ultimately, better constrain future carbon cycle projections.

Concluding remarks

The strong El Niño event of 2015-2016 provided us with an opportunity to study how the global carbon cycle responds to changes in the physical climate system. With the high-resolution (both spatial and temporal) observations available from OCO-2, we are able to directly: (a) observe the strong correlations that exist between atmospheric CO_2 concentrations and the El Niño signal, and (b) track the development of the atmospheric CO_2 anomaly as it switches from a negative phase (i.e., due to a reduction in CO_2 outgassing from the tropical Pacific Ocean) to a strong positive phase (i.e., due to a reduction in biospheric uptake and increased fire emissions). The most important contribution of the space-based OCO-2 mission is the ability to observe and monitor carbon cycle phenomena at high-density over large spatial scales, which has not been possible from the existing *in situ* network.

The complexity of the El Niño – CO_2 signature illustrates that it is a multifaceted system with contributions from many regions and processes. Understanding and predicting its behavior requires separating out the many terrestrial and marine regions that contribute (*1*, *33*) and identifying both the geophysical (*3*, *27, 30*) and the biological (*10*, *59*, *89*) phenomena that respond in their own unique ways. However, the impact on the carbon cycle is unified through the global mixing of CO_2 in the atmosphere - OCO-2 makes a unique contribution by providing both the global coverage and fine surface spatial detail; alongside the *in situ* CO_2 network of moorings and shipboard measurements provide the long-term climate-quality record of atmospheric and ocean CO_2 observations and serves to validate the OCO-2 observations and model products. We emphasize that this diverse observing portfolio is necessary, and the complementary information provided by these observing systems will likely prove critical in understanding the partitioning of carbon fluxes during the 2015-2016 El Niño, the relative contribution of ocean vs. land to the global atmospheric CO_2 growth rate, and the sensitivity of the carbon cycle to climate forcing on interannual to decadal timescales.

References and Notes:

1. M. J. McPhaden, S. E. Zebiak, M. H. Glantz, ENSO as an integrating concept in Earth science. *Science* **314**, 1740-1745 (2006).
2. S. G. Philander, *El Niño, La Niña, and the Southern Oscillation* (Academic Press, San Diego, CA, 1990).
3. J. D. Neelin *et al.*, ENSO theory. *Journal of Geophysical Research-Oceans* **103**, 14261-14290 (1998).
4. K. E. Trenberth, The definition of El Niño. *Bulletin of the American Meteorological Society* **78**, 2771-2777 (1997).
5. M. A. Cane, The evolution of El Niño, past and future. *Earth and Planetary Science Letters* **230**, 227-240 (2005).
6. R. B. Bacastow *et al.*, Atmospheric carbon-dioxide, the southern oscillation, and the weak 1975 El-Niño. *Science* **210**, 66-68 (1980).
7. C. D. Keeling, R. Revelle, Effects of El-Niño Southern Oscillation on the atmospheric content of carbon dioxide. *Meteoritics* **20**, 437-450 (1985).
8. C. D. Keeling *et al.*, Interannual extremes in the rate of rise of atmospheric carbon dioxide since 1980. *Nature* **375**, 666-670 (1995).
9. F. P. Chavez *et al.*, Biological and chemical response of the equatorial Pacific Ocean to the 1997-98 El Niño. *Science* **286**, 2126-2131 (1999).
10. R. A. Feely *et al.*, Influence of El Niño on the equatorial Pacific contribution to atmospheric CO_2 accumulation. *Nature* **398**, 597-601 (1999).

11. R. A. Feely *et al.*, Seasonal and interannual variability of CO_2 in the equatorial Pacific. *Deep-Sea Research Part II-Topical Studies in Oceanography* **49**, 2443-2469 (2002).
12. R. A. Feely *et al.*, Decadal variability of the air-sea CO_2 fluxes in the equatorial Pacific Ocean. *Journal of Geophysical Research-Oceans* **111**, 16 (2006).
13. P. J. Rayner, R. M. Law, R. Dargaville, The relationship between tropical CO_2 fluxes and the El Niño-Southern Oscillation. *Geophysical Research Letters* **26**, 493-496 (1999).
14. C. D. Jones *et al.*, The carbon cycle response to ENSO: A coupled climate-carbon cycle model study. *Journal of Climate* **14**, 4113-4129 (2001).
15. P. Peylin *et al.*, Multiple constraints on regional CO_2 flux variations over land and oceans. *Global Biogeochemical Cycles* **19**, 21 (2005).
16. K. R. Gurney *et al.*, Interannual variations in continental-scale net carbon exchange and sensitivity to observing networks estimated from atmospheric CO_2 inversions for the period 1980 to 2005. *Global Biogeochemical Cycles* **22**, 17 (2008).
17. C. D. Nevison *et al.*, Contribution of ocean, fossil fuel, land biosphere, and biomass burning carbon fluxes to seasonal and interannual variability in atmospheric CO_2. *Journal of Geophysical Research-Biogeosciences* **113**, 21 (2008).
18. X. Jiang *et al.*, Interannual variability of mid-tropospheric CO_2 from Atmospheric Infrared Sounder. *Geophysical Research Letters* **37**, 5 (2010).
19. R. Betts *et al.*, El Niño and a record CO_2 rise. *Nature Climate Change* **6**, 806-810 (2016)
20. P. M. Cox *et al.*, Sensitivity of tropical carbon to climate change constrained by carbon dioxide variability. *Nature* **494**, 341-344 (2013).
21. S. Wenzel *et al*., Emergent constraints on climate-carbon cycle feedbacks in the CMIP5

Earth system models. *Journal of Geophysical Research-Biogeosciences* **119**, 794–807 (2014).

22. K. E. Trenberth *et al*., Progress during TOGA in understanding and modeling global teleconnections associated with tropical sea surface temperatures. *Journal of Geophysical Research-Oceans* **103**, 14291–14324 (1998).
23. J. J. Tribbia, "The rudimentary theory of atmospheric teleconnections associated with ENSO" in *Teleconnections Linking Worldwide Climate Anomalies*, M. H. Glantz, R. W. Katz, and N. Nicholls, Eds. (Cambridge University Press, New York, 1991), pp 285–308.
24. L. Resplandy, R. Séférian, L. Bopp, Natural variability of CO_2 and O_2 fluxes: What can we learn from centuries-long climate models simulations? *Journal of Geophysical Research-Oceans* **120**, 384-404 (2015).
25. F. I. Woodward, M. R. Lomas, T. Quaife, Global responses of terrestrial productivity to contemporary climatic oscillations. *Philosophical Transactions of the Royal Society B-Biological Sciences* **363**, 2779-2785 (2008).
26. Y. Le Page *et al.*, Global fire activity patterns (1996-2006) and climatic influence: an analysis using the World Fire Atlas. *Atmospheric Chemistry and Physics* **8**, 1911-1924 (2008).
27. M. J. McPhaden, COMMENTARY: Playing hide and seek with El Niño. *Nature Climate Change* **5**, 791–795 (2015).
28. A. F. Z. Levine, M. J. McPhaden, How the July 2014 easterly wind burst gave the 2015-2016 El Niño a head start. *Geophysical Research Letters* **43**, 6503 – 6510 (2016).
29. F. Gasparin, D. Roemmich, The strong freshwater anomaly during the onset of the 2015/2016 El Niño. *Geophysical Research Letters* **43**, 6452 – 6460 (2016).

30. H. Paek, J. -Y. Yu, C. Qian, Why were the 2015/2016 and 1997/1998 extreme El Niños different? *Geophysical Research Letters* **44**, 1848-1856 (2017).
31. R. B. Bacastow, Modulation of atmospheric carbon dioxide by southern oscillation. *Nature* **261**, 116-118 (1976).
32. R. E. Newell, B. C. Weare, A relationship between atmospheric carbon dioxide and Pacific sea surface temperatures. *Geophysical Research Letters* **4**, 1–2 (1977).
33. J. L. Sarmiento, N. Gruber, "Carbon Cycle, CO_2 and Climate" in Ocean Biogeochemical Dynamics (Princeton University Press, Princeton, NJ, 2006) pp. 392-453.
34. A. C. Manning *et al.*, Interpreting the seasonal cycles of atmospheric oxygen and carbon dioxide concentrations at American Samoa Observatory. *Geophysical Research Letters* **30**, 4 (2003).
35. R. A. Feely *et al.*, Effects of wind speed and gas exchange parameterizations on the air-sea CO_2 fluxes in the equatorial Pacific Ocean. *Journal of Geophysical Research-Oceans* **109**, 10 (2004).
36. M. Ishii *et al.*, Air-sea CO_2 flux in the Pacific Ocean for the period 1990-2009. *Biogeosciences* **11**, 709-734 (2014).
37. C. D. Jones, P. M. Cox, On the significance of atmospheric CO_2 growth rate anomalies in 2002-2003. *Geophysical Research Letters* **32**, 4 (2005).
38. A. J. Sutton *et al.*, Natural variability and anthropogenic change in equatorial Pacific surface ocean pCO_2 and pH. *Global Biogeochemical Cycles* **28**, 131-145 (2014).
39. A. J. Sutton *et al.*, A high-frequency atmospheric and seawater pCO_2 data set from 14 open-ocean sites using a moored autonomous system. *Earth System Science Data* **6**, 353-366 (2014).

40. R. A. Feely *et al.*, Distribution of chemical tracers in the eastern equatorial pacific during and after the 1982-1983 El Niño southern oscillation event. *Journal of Geophysical Research-Oceans* **92**, 6545-6558 (1987).
41. R. A. Feely *et al.*, Variability of CO_2 distributions and sea-air fluxes in the central and eastern equatorial Pacific during the 1991-1994 El Niño. *Deep-Sea Research Part II-Topical Studies in Oceanography* **44**, 1851-1867 (1997).
42. H. Hashimoto *et al.*, El Niño-Southern Oscillation-induced variability in terrestrial carbon cycling. *Journal of Geophysical Research-Atmospheres* **109**, 8 (2004).
43. P. K. Patra *et al.*, Role of biomass burning and climate anomalies for land-atmosphere carbon fluxes based on inverse modeling of atmospheric CO_2. *Global Biogeochemical Cycles* **19**, 10 (2005).
44. G. R. van der Werf *et al.*, Interannual variability in global biomass burning emissions from 1997 to 2004. *Atmospheric Chemistry and Physics* **6**, 3423-3441 (2006).
45. H. Qian, R. Joseph, N. Zeng, Response of the terrestrial carbon cycle to the El Niño-Southern Oscillation. *Tellus Series B-Chemical and Physical Meteorology* **60**, 537-550 (2008).
46. W. H. Li *et al.*, Impact of two different types of El Niño events on the Amazon climate and ecosystem productivity. *Journal of Plant Ecology* **4**, 91-99 (2011).
47. T. Iguchi, Correlations between interannual variations of simulated global and regional CO_2 fluxes from terrestrial ecosystems and El Niño Southern Oscillation. *Tellus Series B-Chemical and Physical Meteorology* **63**, 196-204 (2011).

48. W. L. Wang *et al.*, Variations in atmospheric CO_2 growth rates coupled with tropical temperature. *Proceedings of the National Academy of Sciences of the United States of America* **110**, 13061-13066 (2013).
49. W. R. L. Anderegg *et al.*, Tropical nighttime warming as a dominant driver of variability in the terrestrial carbon sink. *Proceedings of the National Academy of Sciences of the United States of America* **112**, 15591-15596 (2015).
50. P. Bousquet *et al.*, Regional changes in carbon dioxide fluxes of land and oceans since 1980. *Science* **290**, 1342-1346 (2000).
51. C. R. Schwalm *et al.*, Does terrestrial drought explain global CO_2 flux anomalies induced by El Niño? *Biogeosciences* **8**, 2493-2506 (2011).
52. A. M. E. Winguth *et al*., El Niño Southern Oscillation related fluctuations of the marine carbon cycle. *Global Biogeochemical Cycles* **8**, 39-63 (1994).
53. R. A. Feely *et al.*, CO_2 distributions in the equatorial Pacific during the 1991–1992 ENSO event. *Deep-Sea Research Part II-Topical Studies in Oceanography* **42**, 365–386 (1995).
54. C. Le Quere *et al.*, Interannual variability of the oceanic sink of CO_2 from 1979 through 1997. *Global Biogeochemical Cycles* **14**, 1247-1265 (2000).
55. M. J. Behrenfeld *et al.*, Biospheric primary production during an ENSO transition. *Science* **291**, 2594-2597 (2001).
56. G. A. McKinley *et al.*, Pacific dominance to global air-sea CO_2 flux variability: A novel atmospheric inversion agrees with ocean models. *Geophysical Research Letters* **31**, 4 (2004).

57. T. Takahashi *et al.*, Climatological mean and decadal change in surface ocean pCO_2, and net sea-air CO_2 flux over the global oceans. *Deep-Sea Research Part II-Topical Studies in Oceanography* **56**, 554-577 (2009).
58. G. H. Park *et al.*, Variability of global net sea-air CO_2 fluxes over the last three decades using empirical relationships. *Tellus Series B-Chemical and Physical Meteorology* **62**, 352-368 (2010).
59. M. M. Gierach *et al.*, Biological response to the 1997-98 and 2009-10 El Niño events in the equatorial Pacific Ocean. *Geophysical Research Letters* **39**, 6 (2012).
60. R. Wanninkhof *et al.*, Global ocean carbon uptake: magnitude, variability and trends. *Biogeosciences* **10**, 1983-2000 (2013).
61. M. C. Long *et al.*, Twentieth-Century Oceanic Carbon Uptake and Storage in CESM1(BGC). *Journal of Climate* **26**, 6775-6800 (2013).
62. P. Landschützer *et al.*, Recent variability of the global ocean carbon sink. *Global Biogeochemical Cycles* **28**, 927–949 (2014).
63. P. Landschützer, N. Gruber, D. C. E. Bakker, Decadal variations and trends of the global ocean carbon sink. *Global Biogeochemical Cycles* **30**, 1-22 (2016).
64. C. Rödenbeck *et al.*, Interannual sea-air CO_2 flux variability from an observation-driven ocean mixed-layer scheme. *Biogeosciences* **11**, 4599–4613 (2014).
65. V. K. Valsala *et al.*, Spatiotemporal characteristics of seasonal to multidecadal variability of pCO_2 and air-sea CO_2 fluxes in the equatorial Pacific Ocean. *Journal of Geophysical Research-Oceans* **119**, 8987-9012 (2014).

66. X. J. Wang *et al.*, Seasonal to decadal variations of sea surface pCO_2 and sea-air CO_2 flux in the equatorial oceans over 1984-2013: A basin-scale comparison of the Pacific and Atlantic Oceans. *Global Biogeochemical Cycles* **29**, 597-609 (2015).
67. A. Obata, Y. Kitamura, Interannual variability of the sea-air exchange of CO_2 from 1961 to 1998 simulated with a global ocean circulation-biogeochemistry model. *Journal of Geophysical Research* **108**, 3337 (2003).
68. A. Kuze *et al.*, Thermal and near infrared sensor for carbon observation Fourier-transform spectrometer on the Greenhouse Gases Observing Satellite for greenhouse gases monitoring. *Applied Optics* **48**, 6716-6733 (2009).
69. D. Crisp *et al*., The on-orbit performance of the Orbiting Carbon Observatory-2 (OCO-2) instrument and its radiometrically calibrated products. *Atmospheric Measurement Techniques* **10**, 59-81 (2017).
70. A. E. Eldering *et al.*, The Orbiting Carbon Observatory-2: first 18 months of science data products. *Atmospheric Measurement Techniques* **10**, 549-563, (2017).
71. D. Wunch *et al.*, Comparisons of the Orbiting Carbon Observatory-2 (OCO-2) X_{CO2} measurements with TCCON. *Atmospheric Measurement Techniques* **10**, 2209-2238, (2017).
72. M. J. McPhaden *et al.*, The tropical ocean global atmosphere observing system: A decade of progress. *Journal of Geophysical Research-Oceans* **103**, 14169-14240 (1998).
73. T. Takahashi *et al.*, Decadal variation of the surface water pCO_2 in the western and central equatorial Pacific. *Science* **302**, 852–856 (2003).
74. S. E. Page *et al.*, The amount of carbon released from peat and forest fires in Indonesia during 1997. *Nature* **420**, 61-65 (2002).

75. R. L. Langenfelds *et al.*, Interannual growth rate variations of atmospheric CO_2 and its delta C-13, H-2, CH_4, and CO between 1992 and 1999 linked to biomass burning. *Global Biogeochemical Cycles* **16**, 1048-1069 (2002).
76. G. R. van der Werf *et al.*, Continental-scale partitioning of fire emissions during the 1997 to 2001 El Niño/La Nina period. *Science* **303**, 73-76 (2004).
77. R. J. Parker *et al.*, Atmospheric CH_4 and CO_2 enhancements and biomass burning emission ratios derived from satellite observations of the 2015 Indonesian fire plumes. *Atmospheric Chemistry and Physics* **16**, 10111-10131 (2016).
78. V. Huijnen *et al.*, Fire carbon emissions over maritime southeast Asia in 2015 largest since 1997. *Scientific Reports* **6**, 8 (2016).
79. R. D. Field *et al*., Indonesian fire activity and smoke pollution in 2015 show persistent nonlinear sensitivity to El Niño-induced drought. *Proceedings of the National Academy of Sciences of the United States of America* **113**, 9204-9209 (2016).
80. Y. Yin *et al.*, Variability of fire carbon emissions in equatorial Asia and its nonlinear sensitivity to El Niño. *Geophysical Research Letters* **43**, 10472–10479 (2016).
81. T. Schneider, T. Bischoff, G. H. Haug, Migrations and dynamics of the intertropical convergence zone. *Nature* **513**, 45-53 (2014).
82. G. A. McKinley *et al.*, Convergence of atmospheric and North Atlantic carbon dioxide trends on multidecadal timescales. *Nature Geoscience* **4**, 606-610 (2011).
83. N. Lefèvre, G. Caniaux, S. Janicot, A. K. Gueye, Increased CO_2 outgassing in February-May 2010 in the tropical Atlantic following the 2009 Pacific El Niño. *Journal of Geophysical Research-Oceans* **118**, 1645–1657 (2013).

84. S. M. Vicente-Serrano *et al.*, A multiscalar global evaluation of the impact of ENSO on droughts. *Journal of Geophysical Research-Atmospheres* **116**, 23 (2011).
85. J. Liu *et al.*, Contrasting carbon cycle responses of the tropical continents to the 2015 El Niño. *Science* **THIS ISSUE**, xx (xxxx)
86. J. – S. Kug, F. F. Jin, S. An, Two types of El Niño events: cold tongue El Niño and warm pool El Niño. *Journal of Climate* **22**, 1499–1515 (2009).
87. K. Ashok, T. Yamagata, The El Niño with a difference. *Nature* **461**, 481-484 (2009).
88. M. J. McPhaden, T. Lee, D. McClurg, El Niño and its relationship to changing background conditions in the tropical Pacific Ocean. *Geophysical Research Letters* **38**, L15709 (2011).
89. C. Pala, CLIMATE Corals tie stronger El Niños to climate change. *Science* **354**, 1210 (2016).
90. Procedure for generating the X_{CO2} climatology, calculating the anomaly, sensitivity tests to ascertain its robustness, and associated caveats are described in the Materials and Methods in the Supplementary Materials.
91. See the full list at - http://www.esrl.noaa.gov/psd/data/climateindices/list/
92. Data from other TAO locations (for example, at 0°, 110°W) demonstrate the heterogeneity in CO_2 concentrations as we move from west-to-east over the tropical Pacific Ocean. These data can be viewed at - http://www.pmel.noaa.gov/co2/story/OpenOceanMoorings
93. Bacastow (*31*) found the lag between one of the El Niño indices (SOI) and the CO_2 concentration changes to be 2.5 months at Mauna Loa and 6 months at South Pole. Rayner *et al*. (*13*) found in their study that CO_2 data anomalies lag the SOI by one month.

Later Jones *et al*. (*14*) claimed that Mauna Loa CO_2 lagged behind Niño 3 SST anomalies by 3 months. The handful of studies illustrate the range of ENSO indices and atmospheric CO_2 dataset that have been employed; however, all of these studies were impacted by a lack of broad-scale observations over the tropical Pacific during the different phases of an El Niño event. This study provides a refinement of these earlier estimates of the time lags using higher-density space-based observations.

94. D. Crisp *et al*., The orbiting carbon observatory (OCO) mission. *Trace Constituents in the Troposphere and Lower Stratosphere* **34**, 700-709 (2004).

95. R. Pollock *et al.*, The Orbiting Carbon Observatory instrument: performance of the OCO instrument and plans for the OCO-2 instrument. *Proc. SPIE* 7826, *Sensors, Systems and Next Generation Satellites – XIV* **78260W** (2010).

96. T. E. Taylor *et al.*, Orbiting Carbon Observatory-2 (OCO-2) cloud screening algorithms: validation against collocated MODIS and CALIOP data. *Atmospheric Measurement Techniques* **9**, 973–989 (2016).

97. R. Nelson *et al.*, The potential of clear-sky carbon dioxide satellite retrievals. *Atmospheric Measurement Techniques* **9**, 1671–1684 (2016).

98. C. O'Dell *et al.*, The ACOS CO_2 retrieval algorithm – Part 1: Description and validation against synthetic observations. *Atmospheric Measurement Techniques* **5**, 99-121 (2012).

99. D. Crisp *et al.*, The ACOS CO_2 retrieval algorithm--Part II: Global X_{CO2} data characterization. *Atmospheric Measurement Techniques* **5**, 687–707 (2012).

100. J. Worden *et al.*, Evaluation, Validation, And Attribution Of OCO-2 X_{CO2} Uncertainties. *Atmos. Meas. Tech. Disc*. Available at doi:10.5194/amt-2016-175, in

review (2016).

101. H. Lindqvist *et al.*, Does GOSAT capture the true seasonal cycle of carbon dioxide? *Atmospheric Chemistry and Physics* **15**, 13023–13040 (2015).

102. O. Schneising *et al.*, Long-term analysis of carbon dioxide and methane column-averaged mole fractions retrieved from SCIAMACHY. *Atmospheric Chemistry and Physics* **11**, 2863–2880 (2011).

103. J. P. F. Fortuin, H. Kelder, An ozone climatology based on ozonesonde and satellite measurements. *Journal of Geophysical Research-Atmospheres* **103**, 31709 – 31734 (1998).

104. W. J. Randel, F. Wu, A stratospheric ozone profile data set for 1979–2005: Variability, trends, and comparisons with column ozone data. *Journal of Geophysical Research-Atmospheres* **112**, D06313 (2007).

105. R. D. McPeters, G. J. Labow, Climatology 2011: An MLS and sonde derived ozone climatology for satellite retrieval algorithms. *Journal of Geophysical Research-Atmospheres* **117**, D10303 (2012).

106. H. Nguyen, N. Cressie, A. Braverman, Multivariate Spatial Data Fusion for Very Large Remote Sensing Datasets. *Remote Sensing* **9**, 142 (2017).

107. R. F. Weiss, Carbon dioxide in water and seawater: the solubility of a non-ideal gas. *Marine Chemistry* **2**, 203–215 (1974).

108. M. N. Deeter *et al.*, Operational carbon monoxide retrieval algorithm and selected results for the MOPITT instrument. *Journal of Geophysical Research-Atmospheres* **108**, 4399 (2003).

109. L. Emmons *et al.*, Validation of Measurements of Pollution in the Troposphere (MOPITT) CO retrievals with aircraft in situ profiles. *Journal of Geophysical Research-Atmospheres* **109**, 13 (2004).
110. H. M. Worden *et al.*, Decadal record of satellite carbon monoxide observations. *Atmospheric Chemistry and Physics* **13**, 837-850 (2013).
111. Y. Yin *et al.*, Decadal trends in global CO emissions as seen by MOPITT. *Atmospheric Chemistry and Physics* **15**, 13433-13451 (2015).
112. M. N. Deeter *et al.*, The MOPITT Version 6 product: algorithm enhancements and validation. *Atmospheric Measurement Techniques* **7**, 3623-3632 (2014).
113. M. N. Deeter *et al*., Validation and analysis of MOPITT CO observations of the Amazon Basin. *Atmospheric Measurement Techniques* **9**, 3999-4012 (2016).
114. J. F. Lamarque *et al.*, Identification of CO plumes from MOPITT data: Application to the August 2000 Idaho-Montana forest fires. *Geophysical Research Letters* **30**, 1688 (2003).
115. A. Arellano *et al.*, Time-dependent inversion estimates of global biomass-burning CO emissions using Measurement of Pollution in the Troposphere (MOPITT) measurements. *Journal of Geophysical Research-Atmospheres* **111**, D09303 (2006).
116. Z. Jiang *et al*., Impact of model errors in convective transport on CO source estimates inferred from MOPITT CO retrievals. *Journal of Geophysical Research-Atmospheres* **118**, 2073–2083 (2013).
117. J. Worden *et al.*, El Niño, the 2006 Indonesian peat fires, and the distribution of atmospheric methane. *Geophysical Research Letters* **40**, 4938-4943 (2013).
118. R. Wanninkhof, Relationship between the wind speed and gas exchange over the

ocean revisited. *Limnology and Oceanogrophy - Methods* **12**, 351-362 (2014).

119. M. G. Bosilovich *et al.*, "MERRA-2: File Specification" (Tech. Rep. Global Modeling and Assimilation Office, Office Note No. 9, 2016).

120. K. R. Gurney *et al*., TransCom 3 CO_2 inversion intercomparison: 1. Annual mean control results and sensitivity to transport and prior flux information. *Tellus Series B-Chemical and Physical Meteorology* **55**, 555-579 (2003).

121. K. R. Gurney *et al.,* Towards robust regional estimates of CO_2 sources and sinks using atmospheric transport models. *Nature* **415**, 626-630 (2002).

122. P. A. Pickers, A. C. Manning, Investigating bias in the application of curve fitting programs to atmospheric time series. *Atmospheric Measurement Techniques* **8**, 1469-1489 (2015).

123. K. W. Thoning, P. P. Tans, W. D. Komhyr, Atmospheric carbon dioxide at Mauna Loa Observatory, 2. Analysis of the NOAA/GMCC data, 1974-1985. *Journal of Geophysical Research-Atmospheres* **94**, 8549-8565 (1989).

124. W. Ebisuzaki, A Method to Estimate the Statistical Significance of a Correlation When the Data Are Serially Correlated. *Journal of Climate* **10**, 2147-2153 (1997).

Acknowledgements:

This work was supported by funding from the NASA ROSES-2014 Grant/Cooperative Agreement Number NNX15AG92G. A portion of this research was carried out at the Jet Propulsion Laboratory, California Institute of Technology, under a contract with the National Aeronautics and Space Administration. The work of B.B.S was supported by NCAR, which is sponsored by the National Science Foundation. The work of A.J.S. and R.A.F. was funded by the Office of Oceanic and Atmospheric Research (OAR) of the National Oceanic and Atmospheric Administration (NOAA), U.S. Department of Commerce, including resources from the Ocean Observation and Monitoring Division (OOMD) of the Climate Program Office (FundRef number 100007298). This is Pacific Marine Environmental Laboratory Contribution No. 4607.

The OCO-2 and GOSAT-ACOS data were produced by the ACOS/OCO-2 project at the Jet Propulsion Laboratory, California Institute of Technology, and obtained from the free ACOS/OCO-2 data archive maintained at the NASA Goddard Earth Science Data and Information Services Center (https://disc.gsfc.nasa.gov/OCO-2). The MOPITT datasets were obtained from the NASA Langley Research Center Atmospheric Science Data Center (https://eosweb.larc.nasa.gov/project/mopitt/mopitt_table). The authors gratefully acknowledge the National Data Buoy Center for supporting deployment and recovery of the moored pCO_2 systems and maintenance of the TAO buoys.

Finally, the authors would like to acknowledge the comments from the editor and three anonymous reviewers, discussions with Helen Worden (NCAR), John Worden (JPL), Paul Wennberg (Caltech), Steven Pawson (NASA), Stephen Cohn (NASA), Lesley Ott (NASA) and Brad Weir (USRA), and graphic design help from David Hinkle (JPL) and Sterling Spangler (SSAI).

Figures:

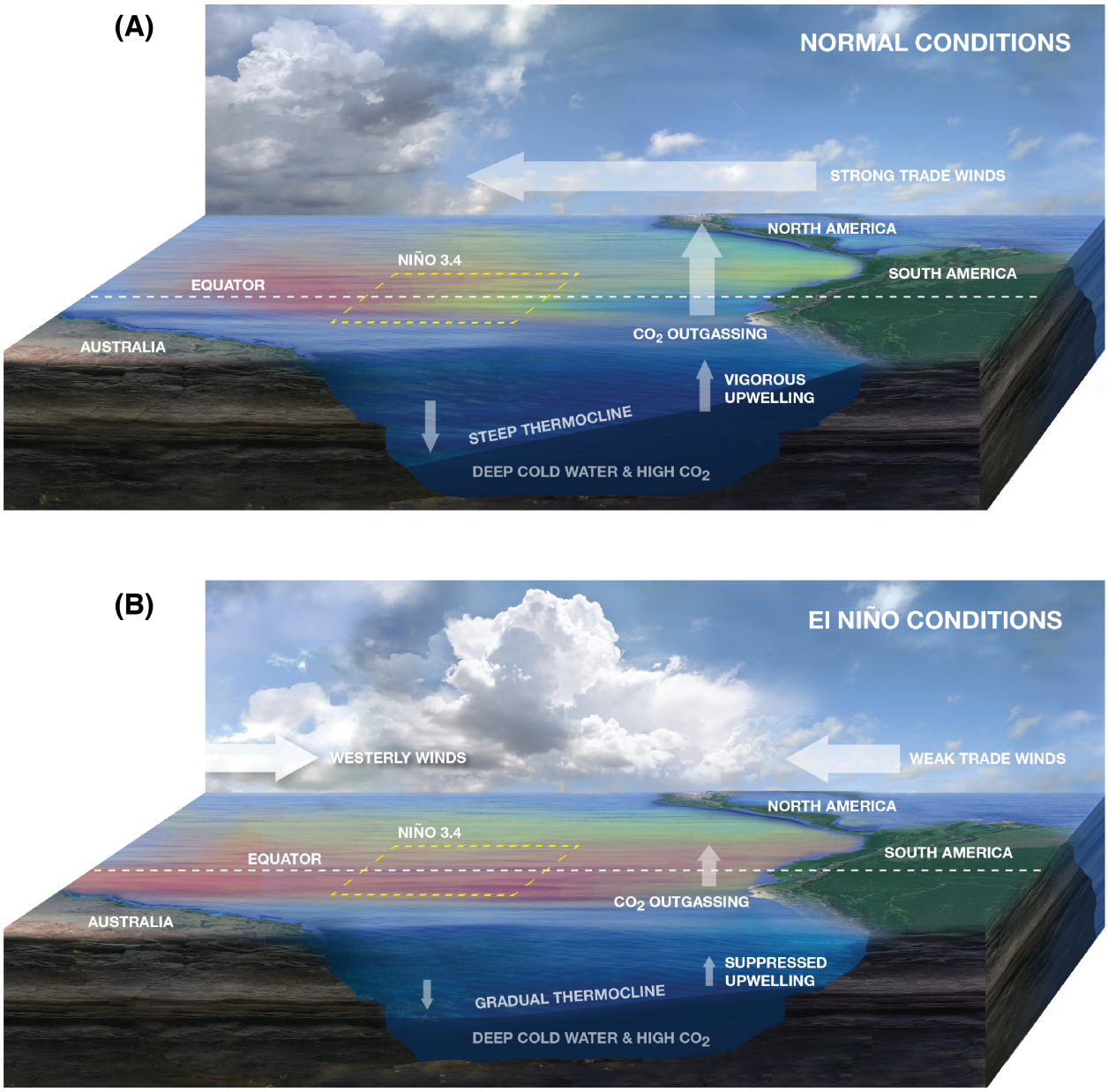
(A)
NORMAL CONDITIONS
STRONG TRADE WINDS
NORTH AMERICA
NIÑO 3.4
EQUATOR
SOUTH AMERICA
AUSTRALIA
CO_2 OUTGASSING
VIGOROUS UPWELLING
STEEP THERMOCLINE
DEEP COLD WATER & HIGH CO_2
(B)
El NIÑO CONDITIONS
WESTERLY WINDS
WEAK TRADE WINDS
NORTH AMERICA
NIÑO 3.4
EQUATOR
SOUTH AMERICA
CO_2 OUTGASSING
AUSTRALIA
SUPPRESSED UPWELLING
GRADUAL THERMOCLINE
DEEP COLD WATER & HIGH CO_2

Fig. 1. Schematic of the mechanistic differences between normal (A) and El Niño (B) conditions and associated carbon response over the tropical Pacific Ocean. Warm ocean surface temperatures are denoted in red and cooler waters in blue. During El Niño conditions, easterly trade winds weaken and westerly wind bursts occur. In association with the shift in wind regimes, the western tropical Pacific warm pool moves eastward and the slope of the thermocline flattens in the central and eastern tropical Pacific. This suppresses upwelling of cold, carbon-rich waters in the central and eastern tropical Pacific, reducing the magnitude of CO_2 outgassing into the atmosphere. Also shown are changes in atmospheric convection, wherein convection shifts eastward in response to eastward displacement of western tropical Pacific warm pool waters.

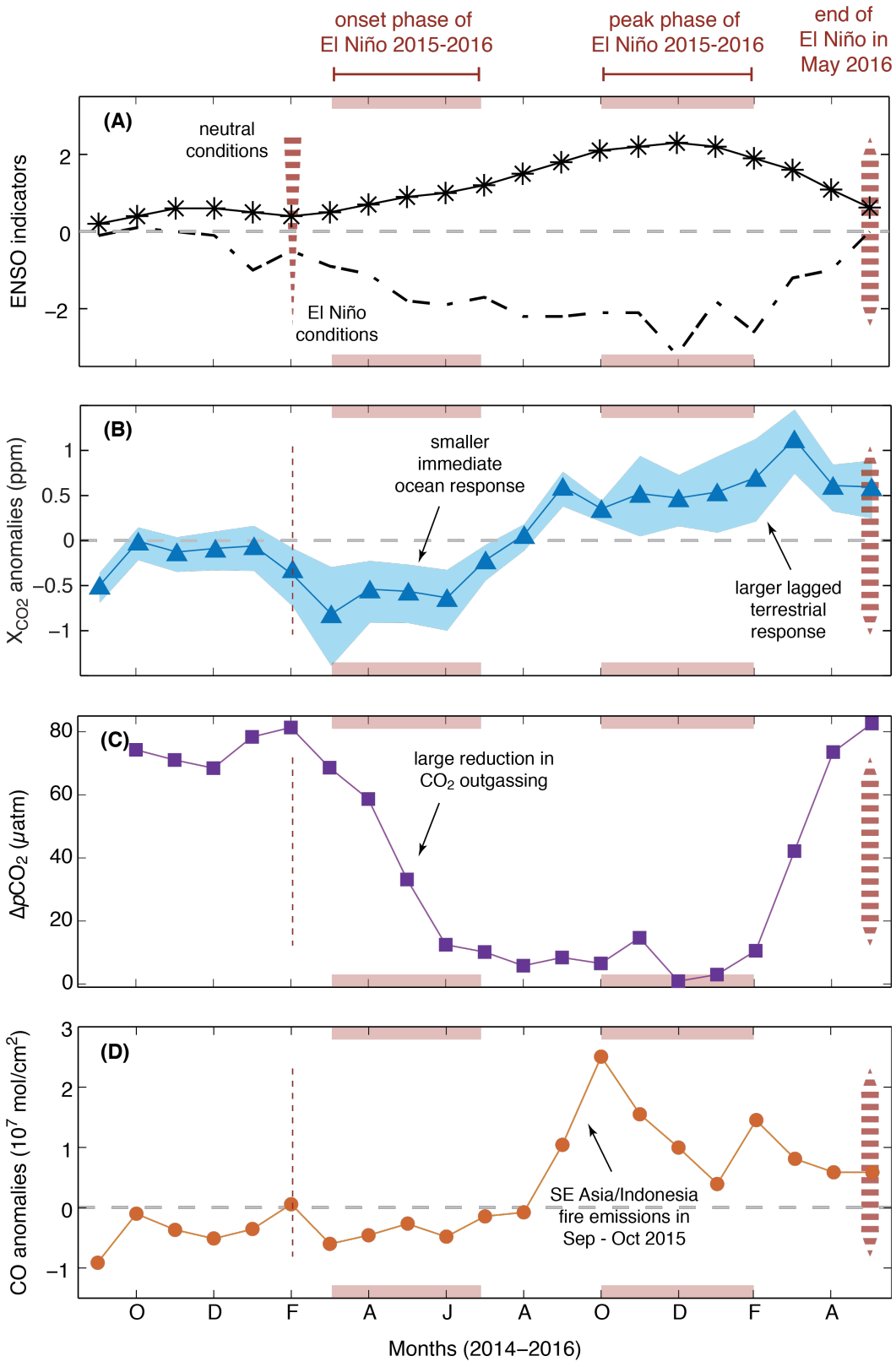
onset phase of El Niño 2015-2016
peak phase of El Niño 2015-2016
end of El Niño in May 2016
(A)
neutral conditions
El Niño conditions
ENSO indicators
(B)
smaller immediate ocean response
larger lagged terrestrial response
X_{CO2} anomalies (ppm)
(C)
large reduction in CO_2 outgassing
ΔpCO_2 (μatm)
(D)
SE Asia/Indonesia fire emissions in Sep - Oct 2015
CO anomalies (10^7 mol/cm^2)
O D F A J A O D F A
Months (2014–2016)
LEGEND
ONI
SOI
Niño 3.4 X_{CO2} anomaly with 1σ uncertainty bounds
Niño 3.4 CO column anomaly
TAO (0°,170°W) ΔpCO_2

1

Fig. 2. OCO-2 observes the response of the carbon cycle for an entire El Niño event. Temporal evolution of (A) the 2015-2016 El Niño as captured by the ONI and the SOI indices, (B) X_{CO2} anomalies and associated uncertainties in the Niño 3.4 region, (C) ΔpCO_2 from the TAO 0°, 170°W mooring, and (D) the CO total column anomalies in the Niño 3.4 region.

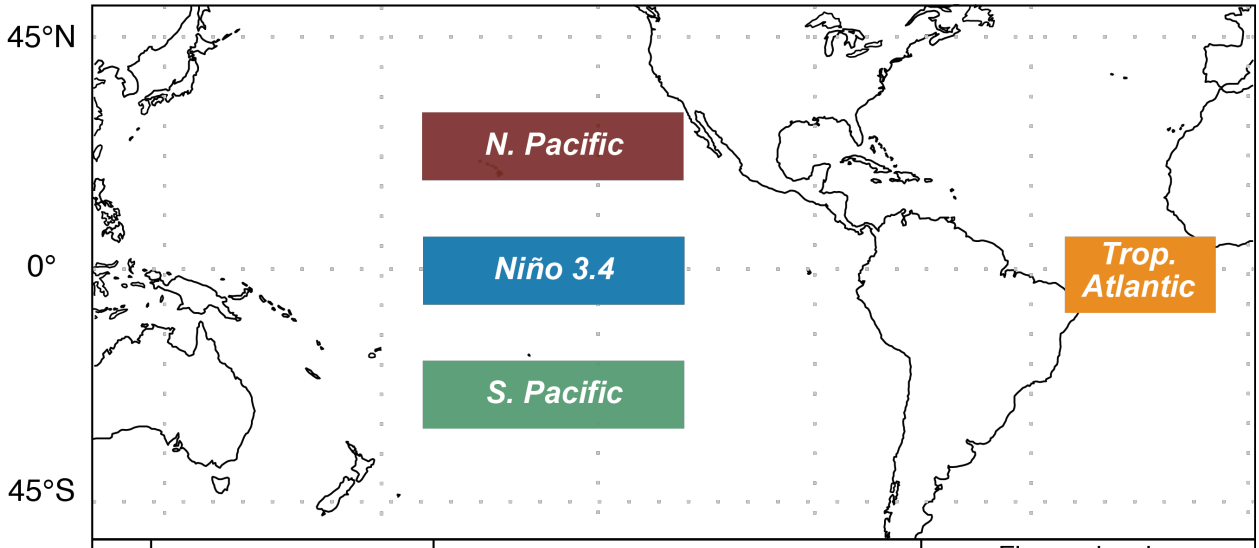

	Specific region analyzed	Alternative hypothesis	Figure showing difference between analyzed region and Niño 3.4
	Global (90°N -90°S, 0°-360°E)	X_{CO2} anomalies over the Pacific Ocean are responding to changes in terrestrial CO_2 concentrations	Fig. 4A
	Tropical Atlantic (5°N -5°S, 5°-35°W)	X_{CO2} anomalies over the Pacific Ocean are responding to changes in global CO_2 concentrations	Fig. 4B
	North Pacific (20°-30°N, 120°-170°W)	X_{CO2} anomalies over the tropical Pacific Ocean are responding to changes in CO_2 concentrations across the entire Pacific Ocean	Fig. 4C
	South Pacific (20°-30°S, 120°-170°W)	X_{CO2} anomalies over the tropical Pacific Ocean are responding to changes in CO_2 concentrations across the entire Pacific Ocean	Fig. 4C

1

Fig. 3. Schematic showing the specific ocean basins (Niño 3.4, N. Pacific, S. Pacific and Trop. Atlantic) that were analyzed in this study. X_{CO2} anomalies are calculated for these different ocean basins, and subsequently compared to the X_{CO2} anomalies from the Niño 3.4 region. Each of these regions was considered to accept/reject a specific hypothesis that could potentially bias the observed trend in the Niño 3.4 X_{CO2} anomalies. After rejecting these hypotheses, we conclude that the negative X_{CO2} anomaly observed over the Niño 3.4 during the onset phase of El Niño 2015-2016 is unique and has to be driven by local changes in the ocean fluxes.

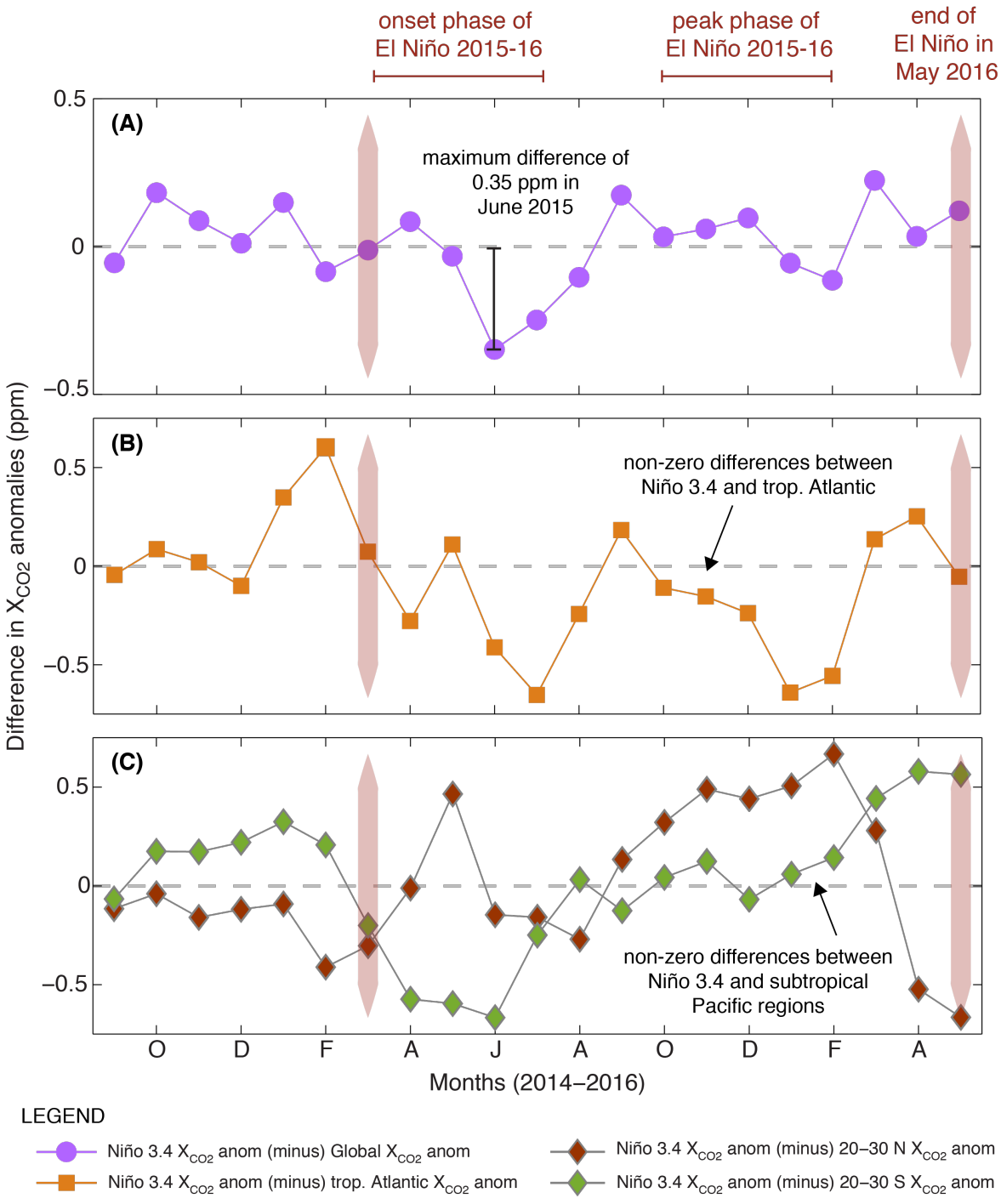
onset phase of
El Niño 2015-16
peak phase of
El Niño 2015-16
end of
El Niño in
May 2016
(A)
maximum difference of
0.35 ppm in
June 2015
(B)
non-zero differences between
Niño 3.4 and trop. Atlantic
(C)
non-zero differences between
Niño 3.4 and subtropical
Pacific regions
0.5
0
−0.5
O
D
F
A
J
A
O
D
F
A
Months (2014–2016)
Difference in X_{CO2} anomalies (ppm)
LEGEND
Niño 3.4 X_{CO2} anom (minus) Global X_{CO2} anom
Niño 3.4 X_{CO2} anom (minus) trop. Atlantic X_{CO2} anom
Niño 3.4 X_{CO2} anom (minus) 20–30 N X_{CO2} anom
Niño 3.4 X_{CO2} anom (minus) 20–30 S X_{CO2} anom

1

Fig. 4. Difference in X_{CO2} anomalies between the Niño 3.4 region and (A) the globe, (B) the tropical Atlantic Ocean, (C) the subtropical Pacific Ocean from September 2014 to May 2016. Definitions of the regions are provided in Fig. 3. In Panel (A), we see a robust pattern of negative X_{CO2} anomaly between Niño 3.4 and the globe that is largest in 2015 and well synchronized with the onset phase of El Niño. In Panels (B) and (C), non-zero differences between Niño 3.4 and the other ocean basins indicate that the Niño 3.4 trend is not reproducible in other ocean basins; thus, allowing us to attribute the negative anomaly in Fig. 2B to a reduction in local CO_2 outgassing over the tropical Pacific Ocean.

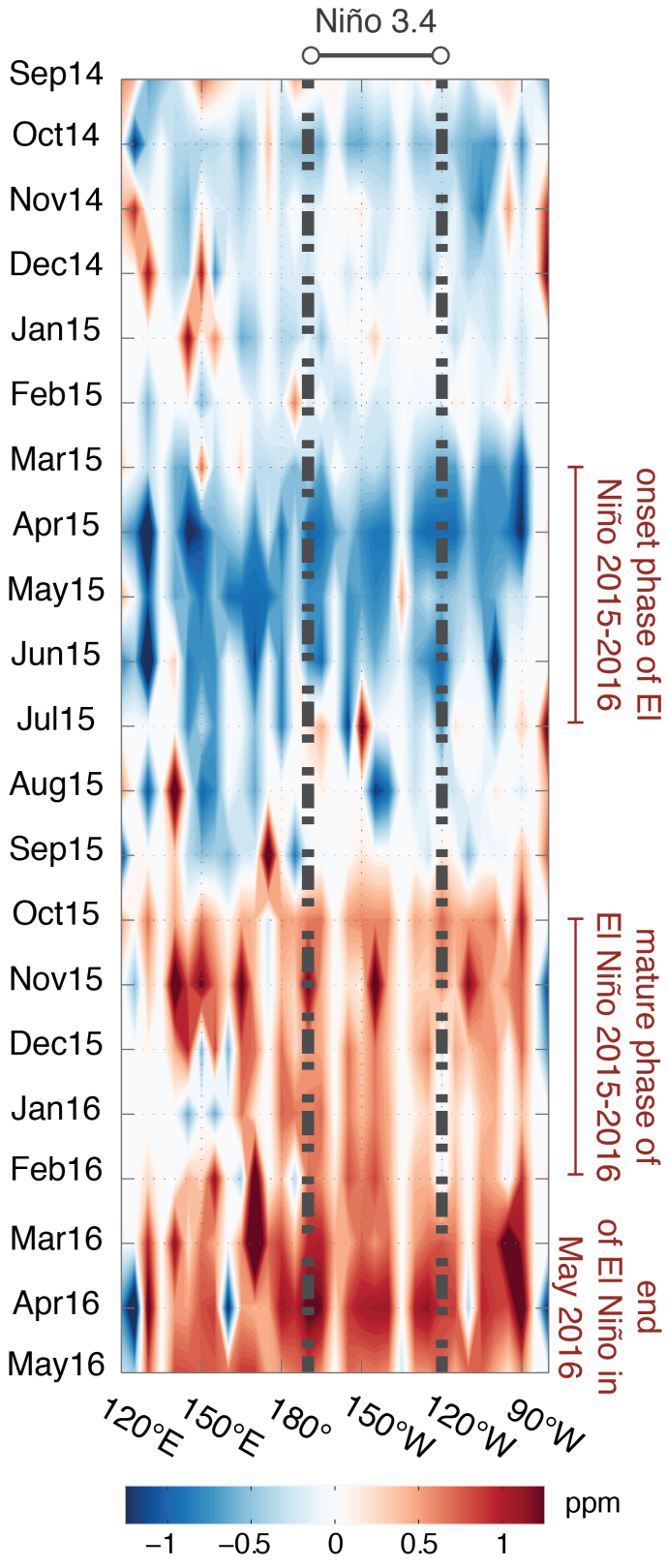
Niño 3.4
Sep14
Oct14
Nov14
Dec14
Jan15
Feb15
Mar15
Apr15
May15
Jun15
Jul15
Aug15
Sep15
Oct15
Nov15
Dec15
Jan16
Feb16
Mar16
Apr16
May16
120°E
150°E
180°
150°W
120°W
90°W
onset phase of El Niño 2015-2016
mature phase of El Niño 2015-2016
end of El Niño in May 2016
ppm
−1
−0.5
0
0.5
1

1

Fig. 5. Time evolution of the X_{CO2} anomalies (ppm) averaged over 5°S-5°N. The x-axis represents longitude and the y-axis shows the time progressing from top to bottom in months. The 2015-2016 El Niño event and its onset and mature phases are highlighted to show the distinct responses observed over the tropical Pacific Ocean. The grey dashed lines capture the boundaries of the Niño 3.4 region. During the onset phase (i.e., March – July 2015), perceptible gradients are observable from the far western Pacific to the central Pacific (consistent with the increasing flux from west to east) along with high variability in the X_{CO2} anomalies in the central Pacific. We also notice that the X_{CO2} anomalies are smaller over the eastern Pacific, which is consistent with surface seawater pCO_2 data collected on the TAO buoys (*92*). The transition from the ocean to the terrestrial signal happens between July and October 2015. Towards the latter stages of the El Niño event (i.e., November 2015 and later), the terrestrial signal dominates the observed trends in X_{CO2} likely masking any underlying ocean signal.

Supplementary Materials for

Influence of El Niño on atmospheric CO_2 over the tropical Pacific Ocean: findings from NASA's Orbiting Carbon Observatory-2 (OCO-2) mission

A. Chatterjee, M. M. Gierach, A. J. Sutton, R. A. Feely, D. Crisp, A. Eldering, M. R. Gunson, C. W. O'Dell, B. B. Stephens, D. S. Schimel

*Correspondence should be addressed to: abhishek.chatterjee@nasa.gov

This PDF file includes:

Materials and Methods

X_{CO2} retrievals from OCO-2 and GOSAT-ACOS

OCO-2 is NASA's first dedicated satellite mission for measuring column average, atmospheric carbon dioxide (CO_2) dry air mole fraction (X_{CO2}) with the accuracy, resolution, and coverage needed for quantifying CO_2 fluxes (sources and sinks) on regional scales over the globe (*69*, *94-95*). Over the sunlit hemisphere, the OCO-2 mission collects nearly one million soundings per day (24 soundings/second) at approximately 3km^2 nadir resolution. After cloud and aerosol screening, between 7 and 12% of these soundings yield full-column estimates of CO_2 on monthly timescales (*96-97*).

The OCO-2 observing strategy (nadir/glint modes) has been refined over the first two years of operations to improve the measurement coverage and yield, especially over the ocean. The initial observing strategy recorded only glint or nadir observations over the entire sunlit hemisphere for a complete, 16-day, ground-track repeat cycle, and then used the other observing mode in the next 16-day cycle. This approach provided adequate coverage of oceans and continents on monthly timescales. In July 2015, this observation strategy was modified to alternate between glint and nadir observations on alternate orbits to yield more continuous coverage of the entire sunlit hemisphere every day. In November 2015, the observation strategy was further optimized to always-collect glint data on orbits that were primarily over the ocean.

The X_{CO2} retrievals used in this work are based on the version 7B (v7B) Level 2 algorithm. These data are freely available via the Goddard Earth Sciences Data and Information Services Center (GES-DISC) from the start of mission operation. OCO-2 results are also being cross-calibrated and cross-validated with measurements and data products from the Japanese Greenhouse gases Observing SATellite (GOSAT, nicknamed "Ibuki"), so that these two satellite

datasets can be combined to produce a uniform X_{CO2} climate data record for use by the carbon cycle science community. The GOSAT X_{CO2} retrievals used in this study have been generated by version 7.3 (v7.3) of the ACOS algorithm (GOSAT-ACOS, *98-99*). Only the high (H) gain observations are retained from the GOSAT-ACOS dataset. These data are bias-corrected using the same predictors as those used for the OCO-2 v7B dataset.

The X_{CO2} estimates have been validated against results from the Total Carbon Column Observing Network (TCCON) and other standards to assess their accuracy and correct regional scale biases (*71*, *100*). After bias correction and data screening, the median residual bias between OCO-2 and TCCON X_{CO2} estimates are less than 0.5 ppm while the root-mean-square (RMS) differences between the two estimates are typically less than 1.5 ppm (*71*). Direct validation of the OCO-2 X_{CO2} estimates against TCCON sites has only revealed biases beyond 2 ppm for some months at Wollongong, Australia (34°S), whereas Ascension Island (10°S in the Atlantic Ocean) has not revealed any noticeable biases. Since there are no TCCON stations in the tropical Pacific Ocean, we must infer the quality of the ocean data from these validation sites in other ocean basins. The OCO-2 team has also noticed errors in the data over the Southern Hemisphere ocean that have a seasonal dependency. Those data are screened out using an airmass-dependent filter (*70*). Because the evaluation of systematic errors in these satellite retrievals is currently the subject of active research, we have carried out additional sensitivity tests (Section C) to ensure that these errors do not impact the findings in this study.

Typically, the X_{CO2} retrievals are only performed on scenes nearly devoid of cloud and/or optically thick aerosol. Because of this, ENSO-induced changes in cloud patterns may cause slight changes in the locations of OCO-2 measurements, but are not expected to induce additional biases in these measurements. We find that the retrieval algorithm sees enough clear-

sky scenes to consistently generate an adequate number of high-quality soundings for the entire time period of this study. For a typical month (e.g., August 2015), we find that GOSAT-ACOS returns ~10K "good-quality" soundings while OCO-2 returns ~150K "good-quality" soundings globally. For OCO-2, 60% of the retrieved soundings are ocean glint observations. Thus, in August 2015, the total number of ocean glint soundings is ~96K. Both of these space-based missions provide significantly more coverage over the tropical Pacific Ocean relative to the sparse *in situ* monitoring network (Fig. S1). In fact, it is the continuous coverage from GOSAT and OCO-2 that allows us to generate a time series of X_{CO2} over the tropical Pacific Ocean (Fig. S2) – for each month between June 2009 – May 2016 individual good-quality ocean glint soundings over the entire Niño 3.4 region are aggregated to generate a single monthly X_{CO2} estimate over Niño 3.4.

Generation of X_{CO2} anomalies

The time-series of X_{CO2} (and in general, time-series of atmospheric CO_2 concentrations) exhibit both a linear trend and a cyclo-stationary component due to the seasonal cycle (Fig. S2). To account for the seasonality and the upward trend of CO_2, we have adopted a two-step approach: (1) for each month, all X_{CO2} retrievals from GOSAT-ACOS and OCO-2 are averaged over pre-specified domains (e.g., Niño 3.4, tropical Pacific Ocean, tropical Atlantic Ocean, global) assuming no temporal correlation between months, and (2) for an individual month, say August, we find a linear trend that best fits the X_{CO2} data from 7-years of GOSAT-ACOS and OCO-2 observational record for that month, i.e., find the linear trend for August 2009, August 2010, August 2011, August 2012, August 2013, August 2014, August 2015. Residuals from this linear trend (Fig. S3) are the X_{CO2} anomalies that will be analyzed. Note that the first derivative of the trend (slope of the linear regression line) provides an estimate of the monthly X_{CO2} growth rate. Simply comparing the growth rate values with those reported in previous studies delivers a necessary (but not sufficient) sanity check of our methodological framework. We have also explored the sensitivity of our calculated anomalies with respect to existing fitting methods (Section B, Fig. S5) and did not see any significant impact on our findings.

Mathematically, if $e_{mo,yr}$ represents the monthly X_{CO2} anomalies for a given year, then these are derived from Equation S1:

$$e_{mo,yr} = y_{mo,yr} - \hat{y}_{mo,yr} = y_{mo,yr} - (\propto_{mo} + \beta_{mo} x_{yr}) \quad \text{… Equation S1}$$

where, $y_{mo,yr}$= observed monthly X_{CO2} value for a given year, x_{yr} = 1,…, 7 for the 7 years, and α and β are the intercept and slope parameters that are estimated during the linear regression procedure. From a physical standpoint, β_{mo} represents the monthly X_{CO2} growth rate (ppm yr^{-1}) and α_{mo} represents the monthly X_{CO2} offset (ppm) relative to the start of our analyses period in

2009. This approach provides the flexibility of calculating the linear trend over any spatial domain – for example, globally, or over the entire tropical Pacific Ocean or separately for individual Niño regions. On monthly timescales, we do find slight differences in growth rates between the entire tropical Pacific Ocean and individual Niño regions – typically these differences are on the order of 0.01-0.2 ppm yr^{-1}. On average the global growth rates vary between 1.88-2.37 ppm yr^{-1} depending on the season. These numbers are consistent with previous studies (*101-102*) that have attempted to derive space-based X_{CO2} growth rate over various spatial domains (e.g., global vs. Northern Hemisphere vs. Southern Hemisphere).

Due to the short time series of the OCO-2 record, we had to rely on the GOSAT-ACOS dataset to provide a climatological reference. While care was taken to use X_{CO2} that are based on the same retrieval algorithm (OCO-2 v7B and GOSAT-ACOS v7.3), we recognize that stitching together data from two different instruments, i.e., GOSAT- and OCO-2 involves an implicit change in sampling strategy plus changes in observational density. Within the atmospheric trace gas remote-sensing community, this is a strategy that has been employed for generating climatologies from data available over a limited timespan – a typical example being the generation of ozone climatology using profile data from ozonesondes, observations from multiple satellite instruments, etc. (*103-105*). Section C discusses the sensitivity tests we have carried out to confirm that the derived X_{CO2} anomalies are not being impacted due to this '*change of instrument*' issue. In the future, as the OCO-2 data record grows, we will able to revise the climatology based on a homogenous X_{CO2} record, either from actual OCO-2 data or quasi-operational Level-3 maps (*106*) that will be made available as part of the OCO-2 product suite.

pCO_2 observations from the TAO array

The TAO (Tropical Atmosphere Ocean) array of moored buoys in the tropical Pacific Ocean provides real-time, in situ meteorological and oceanographic measurements (*72*). Atmospheric and surface seawater partial pressure of CO_2 (pCO_2) is currently measured by Moored Autonomous pCO_2 ($MAPCO_2$) systems maintained on the TAO array at 0°, 110°W; 0°, 125°W; 0°, 140°W; 0°, 155°W; 0°, 170°W; 0°, 165°E; and 8°S, 165°E (*38*).

In brief, the $MAPCO_2$ system (*39*) utilizes an automated equilibrator-based gas collection system to measure surface seawater xCO_2 (the mole fraction of CO_2 in air in equilibrium with surface seawater) at approximately 14 cm depth and atmospheric xCO_2 at approximately 1.5 m above the sea surface every 3 hours. This xCO_2 (wet) measurement is made by a non-dispersive infrared gas analyzer (LI-820, LI-COR) calibrated before, during, and after field deployment with reference gases traceable to World Meteorological Organization standards prepared by NOAA's Earth System Research Laboratory. The $MAPCO_2$ system also measures sample temperature, pressure, and relative humidity to calculate xCO_2 (dry) based on the equations in (*107*). Sea surface temperature (SST) and salinity from TAO temperature and conductivity sensors are then used to calculate pCO_2 consistent with ocean carbon standard operating procedures as described in (*39*).

Once data are recovered from the field and quality controlled, 3-hourly CO_2 observations are archived at the Carbon Dioxide Information Analysis Center (http://cdiac.ornl.gov/oceans/Moorings/) and the National Centers for Environmental Information (https://www.ncei.noaa.gov/). Monthly averaged real-time observations of ΔpCO_2 (seawater pCO_2 – atmospheric pCO_2) from September 2014 – May 2016 are shown in Fig. 2C and Table S1. Quality control checks on the pCO_2 observations reveal good measurements were

collected during this time period. Based on laboratory tests at NOAA Pacific Marine Environment Laboratory (PMEL) and field intercomparisons, estimates of uncertainty for quality-controlled air and seawater pCO_2 measurements are ≤2 μatm (*39*); however, uncertainty of preliminary monthly-averaged data are likely slightly higher (≤5 μatm). Data plots from all TAO pCO_2 locations, which include both real time and finalized data, are available at - www.pmel.noaa.gov/co2/story/Open+Ocean+Moorings.

Figure 2C captures the temporal trend in the ΔpCO_2 values from the 0°, 170°W TAO array buoy, which is located in the western-most portion of the Niño 3.4 region. Preliminary analyses seem to suggest that this buoy registered the first response to the onset of El Niño conditions. On the other hand, observations at 0°, 110°W from the TAO array buoy (https://www.pmel.noaa.gov/co2/story/Open+Ocean+Moorings) seem to indicate that upwelling of high dissolved inorganic carbon (DIC) water continued in the central and eastern-most portion of the Niño 3.4 region till early Fall 2015 with only brief periods (November 2015 – February 2016) where surface seawater pCO_2 was close to equilibrium with atmospheric values. Observations from these more eastern sites indicate diverse regimes operating across the tropical Pacific; Fig. 5 qualitatively demonstrates that the X_{CO2} anomalies capture these regional gradients depending on its magnitude, seasonality, location, etc. As more *in situ* measurements become available, quantitative investigations are ongoing to check how well the OCO-2 observations can resolve such regional gradients.

CO observations from the MOPITT instrument

Since March 2000, the MOPITT instrument on board the NASA/EOS Terra platform has been monitoring the CO content in the troposphere. Details about the retrieval algorithm, its validation and uncertainties are provided in Deeter *et al*. (*108, 112-113*) and Emmons *et al*. (*109*) while analyses and discussion of decadal CO trends are provided in more recent studies (*110-111*). An instrument cooler failure between May and August 2001 significantly impacted the retrieval mean levels before and after the instrument anomaly. Hence for the sake of homogeneity, we select data during the period June 2002 - May 2016 for generating a climatological value of CO content in the atmosphere. Unlike the shorter X_{CO2} record, the availability of a long and homogeneous CO data record (>14 years) from a single instrument makes the generation of the climatology (and associated anomaly calculations) straightforward. Based on the recommendation of the MOPITT team, we use the Level 3 MOPITTv6 CO (*112*) estimated from the thermal-infrared (TIR) channel. TIR measurements offer the best description of CO emissions from fires due to the large thermal contrast between the lower troposphere and free troposphere due to intense surface heating. For this study, we look at the CO Volume Mixing Ratio (VMR) for both the total column and at an individual atmospheric pressure level at 700 hPa.

Given that the two largest surface sources of CO are the combustion of fossil fuel and the combustion of biomass (forest and savanna fires, biofuel use, and waste burning), MOPITT CO anomalies have been used to track emission from fires, including El Niño-related ones (*114-117*). While the surface level anomalies can detect the onset of fires immediately (i.e., without any time lag), CO anomalies at higher levels in the atmosphere increase gradually and exhibit significantly smaller peak anomaly values than the surface. These features are consistent with the

expected lag and dilution associated with vertical mixing. Fig. S4 shows that the impact of fire emissions between August and October 2015 from S.E. Asia/Indonesia are clearly visible over the tropical Pacific Ocean. The largest anomalous sources of CO occur over the Indonesian regions, which are emitted as strong pulses over the 3-month window. These maps also rule out biomass burning emissions from other regions, such as Africa and South America that can potentially influence the rise in CO and CO_2 concentrations over our region of interest (i.e., Niño 3.4).

Because the signal from enhanced fire emissions are correlated with drought, however, we cannot quantitatively discriminate the relative roles of reduction in biospheric uptake due to warmer, drier climates or emissions from biomass burning by just looking at the trends in the anomalies in the CO_2 and the CO data. What we can discern is the timing of the large tropical source (of which the biomass burning emissions are a major contributor) and its impact on the rise in CO_2 concentration anomalies from August 2015 onwards.

Supporting Text

Section A: Calculation of sea-to-air fluxes from the TAO and the OCO-2 datasets

Calculation of sea-to-air flux from pCO_2 observations

Following Wanninkhof (*118*), the net flux of CO_2 across the air-sea interface, **F** (mass area^{-1} time^{-1}) is calculated as the product of the gas transfer velocity **k** (length time^{-1}), the solubility of CO_2, **s** (mass volume^{-1} pressure^{-1}), and the pCO_2 (pressure) difference between the ocean and atmosphere ($pCO_2^{sw} - pCO_2^{atm}$), according to Equations S2 and S3:

$$\mathbf{F} = \mathbf{ks}(pCO_2^{sw} - pCO_2^{atm}) \quad \text{… Equation S2}$$

$$\mathbf{k} = 0.251\mathbf{U}_{10}^2(S_c/660)^{-0.5} \quad \text{… Equation S3}$$

where, Sc is the Schmidt number for CO_2, and $\mathbf{U}_{10}$ is the wind speed at 10m height. By convention, the units of **k** are in cm h^{-1}, $\mathbf{U}_{10}$ is in m s^{-1} and units of the coefficient 0.251 are (cm h^{-1}) (m s^{-1})$^{-2}$. Daily averaged wind speeds were acquired from the Modern-Era Retrospective analysis for Research and Applications, Version 2, or MERRA-2 (*119*).

Based on these equations, the calculated fluxes at TAO 0°, 170°W are 0.21 ± 0.20 (1σ) gC m^{-2} month^{-1} between April 2015 – March 2016 (i.e., during the El Niño 2015-2016 event). This is a flux reduction of 84% relative to the neutral April 2014 – March 2015 period during which the magnitude of flux was 1.35 ± 0.20 (1σ) gC m^{-2} month^{-1}. Note that this flux difference is only representative of the western-most portion of the Niño 3.4 region. The CO_2 fluxes and the magnitude of flux reduction could be considerably different in the eastern-most portions of the tropical Pacific Ocean. Studies reporting on the magnitude of air-sea flux reduction across the tropical Pacific Ocean during El Niño events typically report a flux reduction of ~40-60%.

Calculation of sea-to-air flux from X_{CO2} observations

Following Gurney *et al*. (*120*), we have used simple atmospheric transport model simulations to assess whether the magnitude of ocean flux anomaly based on the pCO_2 observations is consistent with the anomaly observed in the X_{CO2} estimates. For the 16 models participating in the TransCom3 Level 1 experiment (T3L1) (*121*), we have calculated the average column mean CO_2 enhancement over the Niño 3.4 region for the Eastern Equatorial Pacific basis function (region 14) fluxes. As per the TransCom experiment protocol, the fluxes for this basis function was set to a constant 1 PgC yr^{-1} evenly distributed within the region. These data are precomputed and available as part of the TransCom 3 experiments at - http://transcom.project.asu.edu/transcom03_output.php. The average difference between Niño 3.4 region and a global reference column mean is 0.43 ± 0.09 (1σ) ppm. The global reference is based on a latitudinal cutoff of 60°S-60°N keeping in mind the range of latitudes over which OCO-2 observations are available. Since the basis function used in these experiments was 1 PgC yr^{-1} constant emission, this gives a sensitivity of 1/0.43 = 2.33 PgC yr^{-1} per ppm, or for a 0.26 ± 0.09 (1σ) ppm dip (as seen from Fig. 4A over May, June, July, August 2015) about 0.60 ± 0.21 (1σ) PgC yr^{-1}. Given that the dip in X_{CO2} anomalies are observed over a period 4 months long (Fig. 4A), this would suggest a total flux of 0.20 ± 0.07 (1σ) PgC. As per the TransCom framework, note that this is an implied flux difference, in PgC absolute. Thus, if the original magnitude of sea-to-air flux is 0.5 PgC yr^{-1} (*36*), then the implied reduction in the flux outgassing is 0.2/0.5 * 100 = 40 ± 14 (1σ) % (i.e., 26-54%). This simple but effective calculation provides a necessary sanity check on the magnitude of the signal observed from the X_{CO2} data.

In reality, the changes in the surface fluxes are far more complicated with processes occurring at distinct spatiotemporal scales and with different levels of maturity. The simple

analysis presented here does not take into account spatial gradients in fluxes within the east equatorial Pacific region itself or between the east and west tropical Pacific Ocean, all of which may have been possible for the 2015-2016 El Niño event. More detailed analyses using atmospheric inverse modeling/data assimilation techniques and both satellite and *in situ* data are necessary (and ongoing) to parse out the grid-scale air-sea flux magnitudes over the tropical Pacific Ocean.

Section B: Analyzing the sensitivity of X_{CO2} anomalies to the curve fitting procedure

Pickers and Manning (*122*) discuss that significant bias and uncertainty can be introduced in the application of curve fitting programs to atmospheric time series. The specific curve fitting method used in this study was designed keeping in mind the attributes of atmospheric CO_2 concentrations (i.e., both long-term growth rate and seasonal cycle). In principle, the overall framework is analogous to the one currently used at NOAA ('CCGCRV') to fit observation time series from the NOAA *in situ* network. Originally based on Thoning *et al*. (*123*), the CCGCRV curve fitting method represents the long-term growth rate by a polynomial function, the annual oscillation by harmonics of a yearly cycle and then uses a low pass filter to retain interannual and short term variations in the fitted curve. There is no set rule on the number of polynomial terms in the function, and it depends on the application and user preference.

We have used the CCGCRV curve fitting method to detrend our X_{CO2} time series, and re-calculated the anomalies and the growth rates (Fig. S5). A simple linear term was used for the polynomial part of the function to make the overall function as comparable as possible to our curve fitting method. We find that the overall pattern in the X_{CO2} anomalies (negative anomaly during Summer 2015 followed by a positive anomaly in Fall 2015) is consistent for both methods. This implies that the curve fitting procedure did not introduce any spurious bias or trend onto our analyses.

Section C: Uncertainty analyses for the trend in X_{CO2} anomalies

An ensemble approach is used to quantify the error associated with the time series of the Niño 3.4 X_{CO2} anomaly. Fig. S6 shows specific tracks that GOSAT flies over, and only 6 of those tracks lie within the Niño 3.4 region. We create an ensemble of small regions that are roughly 200 km x 400 km around those individual GOSAT tracks. For each of these regions (30 in total), we apply the same methodology to generate the X_{CO2} climatology and extract the associated anomaly for our study time period (September 2014 – May 2016). The resultant spread among the 30 ensemble members defines the 1σ standard deviation for the mean X_{CO2} anomaly line (Fig. 2B), which is still derived from the full Niño 3.4 region.

We have carried out an additional sensitivity test (Fig. S7) where we have systematically added/subtracted constant mean bias values (0.1-1ppm) to the ocean glint retrievals used in this study. Given the lack of validation data over the tropical Pacific Ocean, it is necessary to ascertain that residual systematic errors in the ocean glint retrievals (*71*, *100*) do not alias onto our calculations. Fig. S7 illustrates that even in the worst-case scenario, where the ocean glint retrievals have a low bias (i.e., negative) of 1 ppm, the overall temporal structure of the X_{CO2} anomaly is conserved. The impact on the X_{CO2} anomaly line is that it shifts up or down depending on the magnitude of the bias, which in turn impacts the inference of the magnitude of the air-sea fluxes. Certainly, a more complicated structure of the residual biases (e.g., coherent spatial and temporal dependency or correlations between biases) will impact these trends in a different manner. But based on our current understanding of the satellite retrievals, these sensitivity tests and the ocean basin-related diagnostics (Figs. 3 and 4) show that the findings are robust to a couple of first order caveats that have not been resolved for the global OCO-2 dataset as a whole.

Section D: Cross-correlation between X_{CO2} anomalies and SST anomalies

We have investigated the cross-correlation between the X_{CO2} anomalies and the ONI index (which are derived from the Niño 3.4 SST anomalies) for the entire period of June 2009 – May 2016 (n=84) to test the magnitude and phase of the relationship between the two variables. The largest correlations are found for X_{CO2} anomalies lagging the ONI by 1-2 months (Fig. S8). These correlations are significant at the 95% level based on the random phase test of Ebisuzaki (*124*). Previous studies (*6*, *13*, *14*, *31*) have looked at carbon cycle related anomalies (i.e., anomalies in CO_2 concentrations or CO_2 fluxes) and tested its phasing and strength with a suite of ENSO indices (e.g., SOI, Niño 3 SST anomalies, etc.). Jones *et al*. (*14*) provides the closest analogy to this work, where they reported a lag of 3 months between the CO_2 concentrations measured at Mauna Loa and Niño 3 (5°S-5°N, 90°W-150°W) SST anomalies.

We believe that the longer response time of the Mauna Loa CO_2 anomalies to SST anomalies is not necessarily a feature of the carbon cycle but rather due to a time lag associated between the driver (SST) and the response (CO_2) measured at a location far away from the center of action. The availability of X_{CO2} retrievals directly over the region of action (tropical Pacific Ocean and the Niño 3.4 region) provides a new tool for understanding both the strength of correlation of atmospheric CO_2 changes with ENSO and the real-time lag associated with the ocean carbon cycle response.

Supporting Figures and Tables

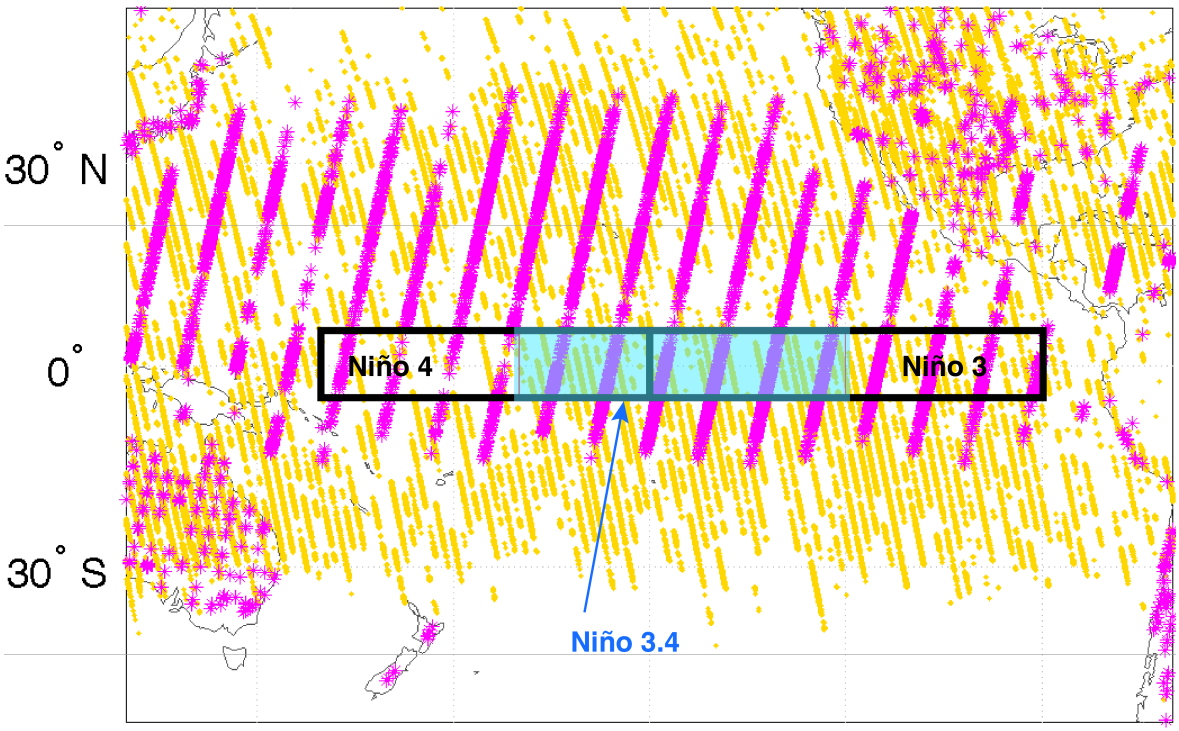

Fig. S1. Coverage over the Pacific Ocean from GOSAT-ACOS v7.3 (magenta) and OCO-2 v7B (gold) for one representative month in 2015. Relative to GOSAT, OCO-2 provides more observations over the open ocean (~100x more soundings per day) with higher accuracy and precision. Also shown are the Niño regions over the tropical Pacific Ocean that are traditionally used to study and define El Niño events.

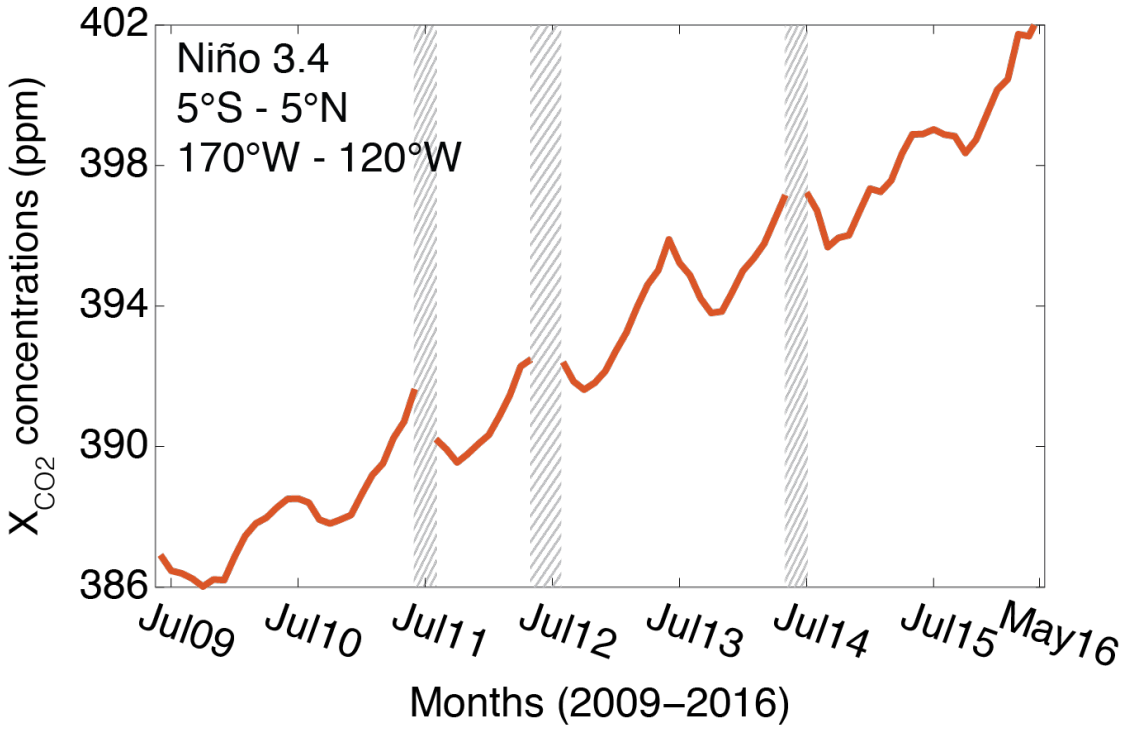

Fig. S2. Time-series of X_{CO2} over the Niño 3.4 region for seven years (June 2009 – May 2016) after combining the GOSAT and the OCO-2 data streams. The availability of space-based observations over remote locations, such as the Niño 3.4 region, allows us to stitch together a long-time series of X_{CO2} concentrations from which the X_{CO2} anomalies can be deduced (Fig. S3). Grey-hatched portions indicate time-periods during which data is not available over the Niño 3.4 region (July 2011, June 2012 – July 2012 and June 2014)– either due to instrument downtime or planned maintenance.

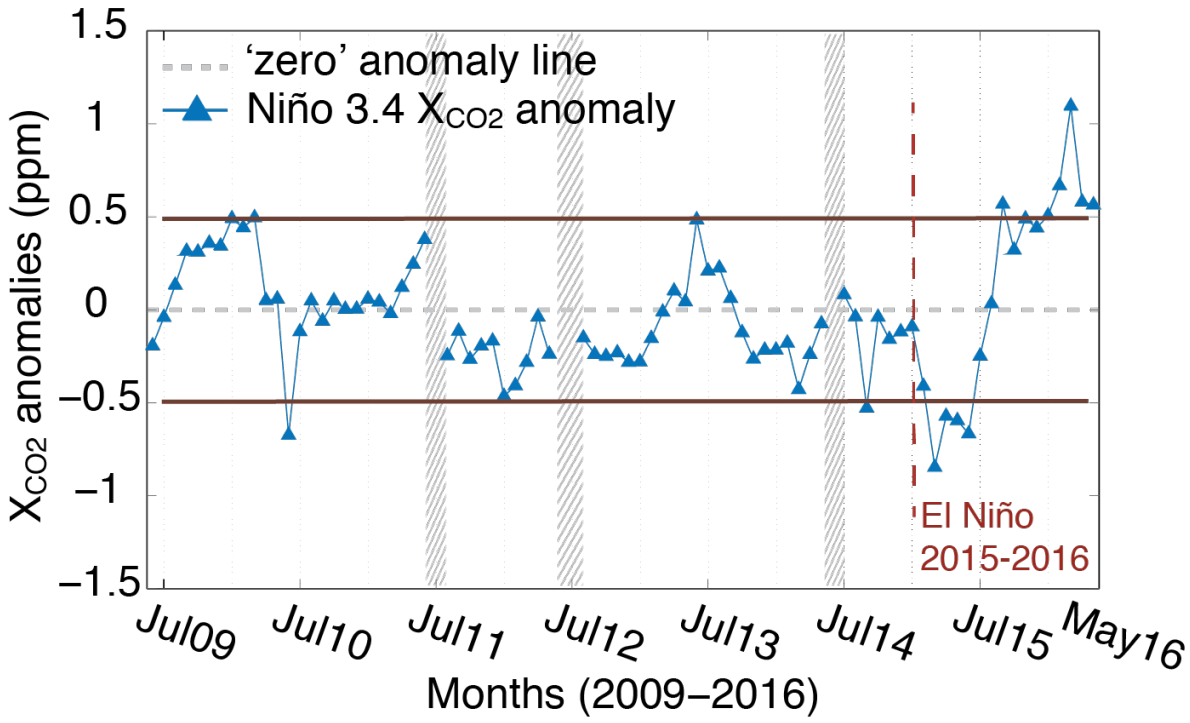

Fig. S3. Multi-year time series of X_{CO2} anomalies over the Niño 3.4 region. The timespan covers June 2009 to May 2016. Grey-hatched portions indicate time-periods during which data is not available over the Niño 3.4 region (July 2011, June 2012 – July 2012 and June 2014)– either due to instrument downtime or planned maintenance. The horizontal brown lines indicate the range of uncertainty (± 0.5 ppm) expected in the X_{CO2} data. The vertical dashed red line shows the time period from which a subset of this time series (September 2014 to May 2016) has been explored in detail in this study. Comparison to previous years illustrates, however, that the anomaly signature observed during the 2015-2016 period are distinct relative to other periods.

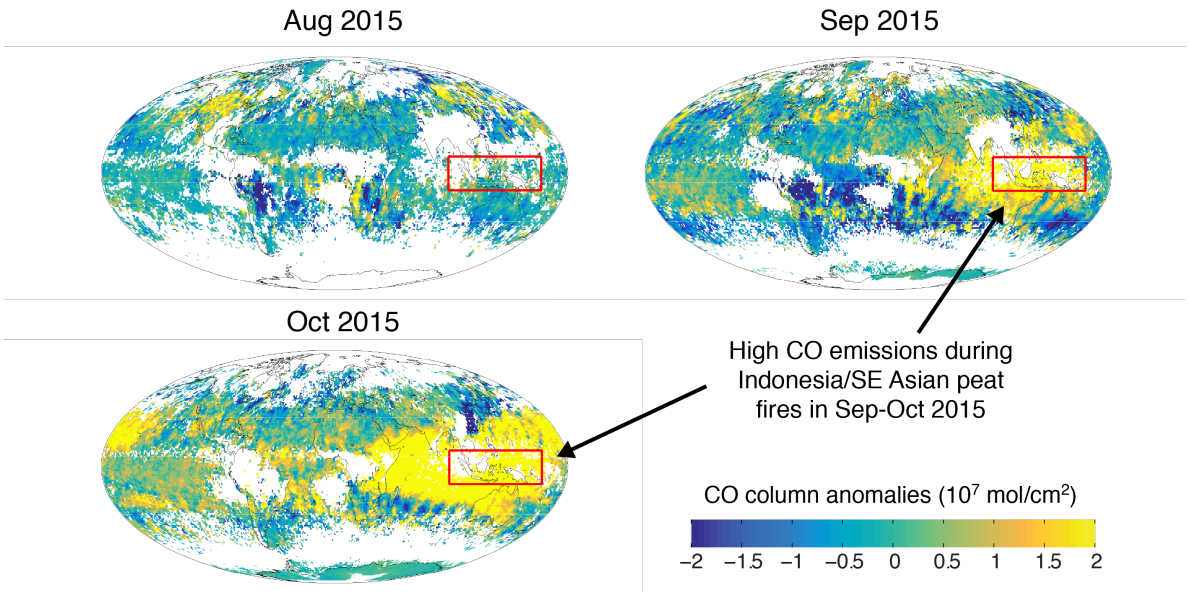

Fig. S4. Spatial distribution of CO total column anomalies retrieved from the MOPITT instrument between August and October 2015. The red rectangle shows the location of SE Asia and Indonesia. Note the spike in CO anomalies during September 2015 due to the Indonesian peat fires, and subsequent advection (visible as a yellow blob) eastward across the tropical Pacific Ocean and westward over the tropical Indian Ocean. The peak values of CO anomalies occur during October 2015, which is also evident from the time series in Fig. 2D.

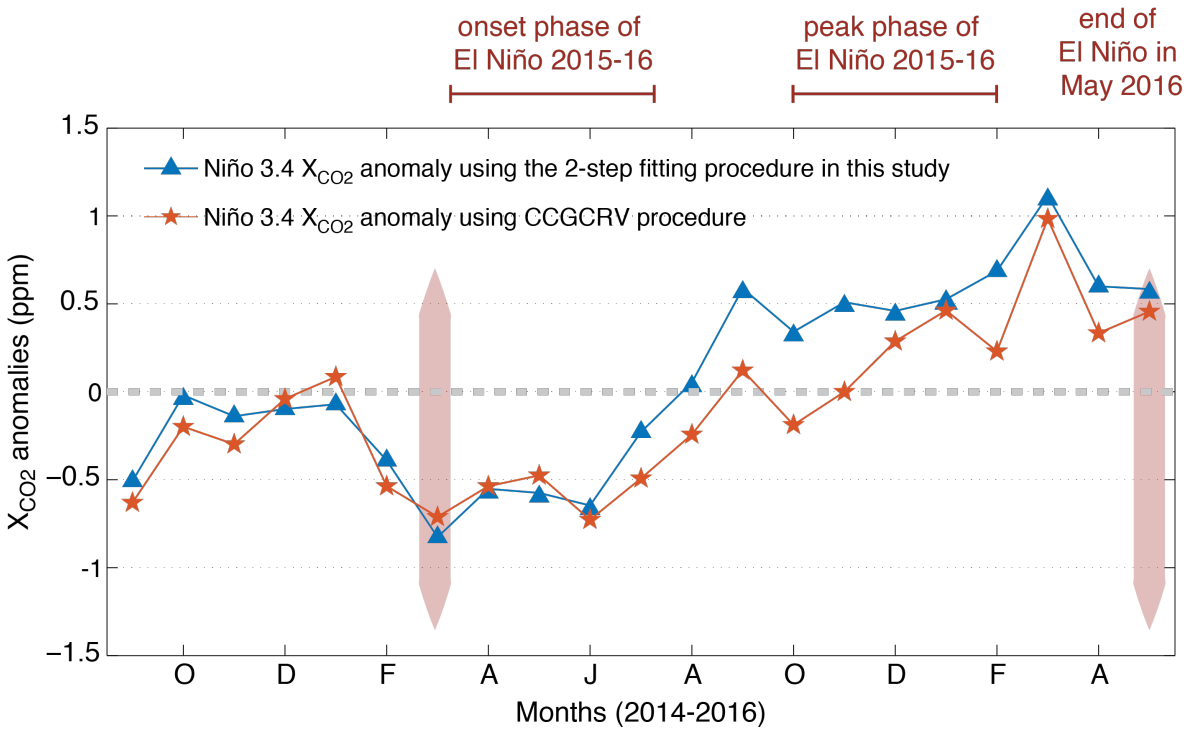

Fig. S5. Time series of X_{CO2} anomalies generated by two different curve-fitting methods – the procedure used in this study (blue line with diamonds) and the traditional 'CCGCRV' procedure (orange line with stars). Both methods generate similar trends in the anomaly during the onset phase (i.e., negative anomaly in X_{CO2}) and the mature phase of El Niño (i.e., steep increase in X_{CO2} anomaly). However, we do note a systematic difference in the magnitude of the positive X_{CO2} anomaly (August – December 2015) likely due to the difference in the number of parameters used in the two curve-fitting procedures.

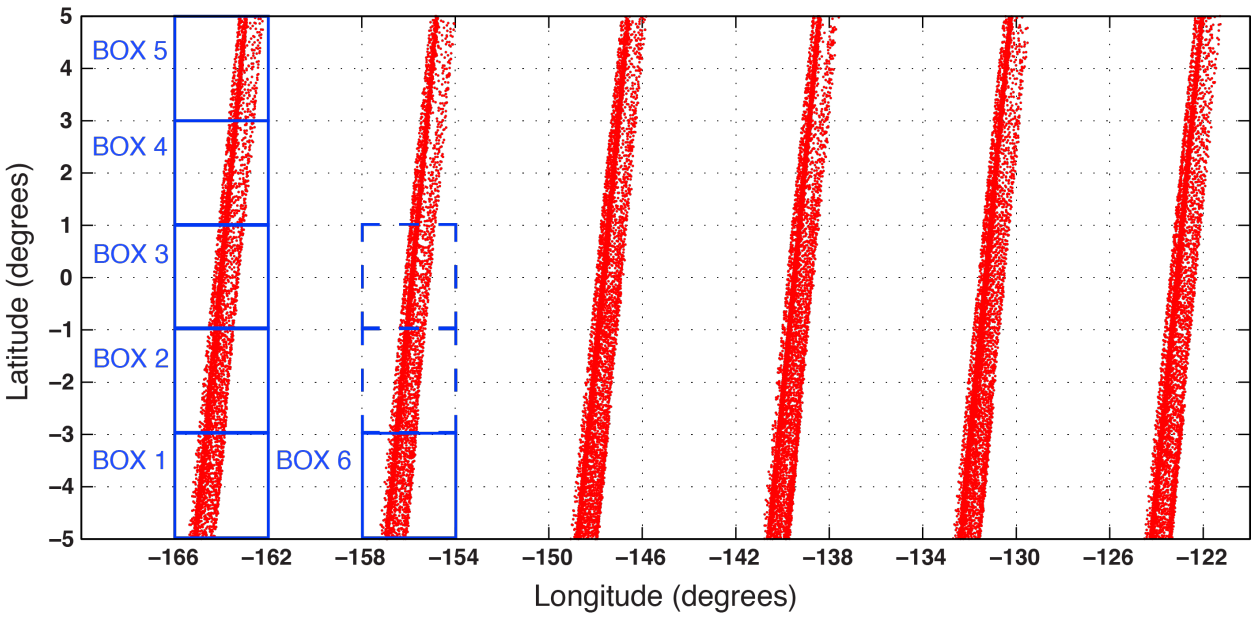

Fig. S6. Schematic of the methodology used to generate an ensemble of boxes within the Niño 3.4 domain. Each individual box is centered around a GOSAT track – this ensures that the spatial coverage provided by the two remote sensing missions (GOSAT and OCO-2) are roughly equivalent within the box, thus minimizing the impact of differences in sampling density between the two instruments.

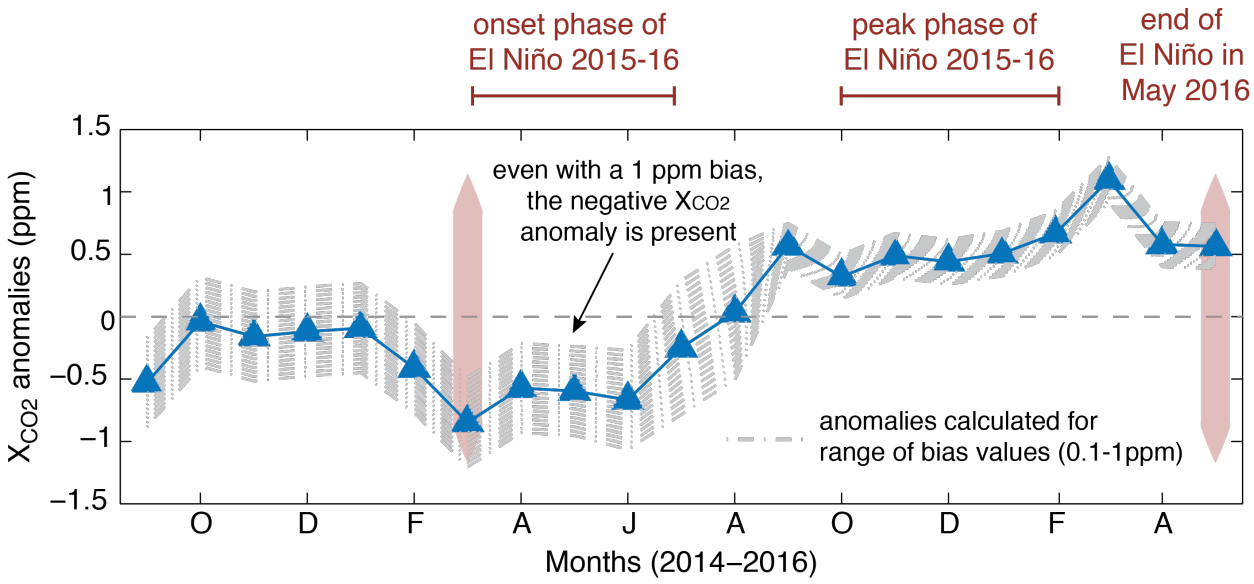

Fig. S7. Uncertainty associated with the X_{CO2} anomaly time series given residual systematic errors in the ocean glint retrievals. A range of constant mean bias values from ± 0.1 to ± 1.0 ppm were added to the ocean glint retrievals from OCO-2, and the X_{CO2} anomaly re-calculated for each bias level. Even in the worst-case scenario (low 1 ppm bias over the tropical Pacific Ocean), the overall temporal structure of the ocean and the terrestrial responses are conserved. The magnitude of the X_{CO2} anomaly shifts upward or downward, which will have consequences for the inferred changes in ocean/land –atmosphere fluxes.

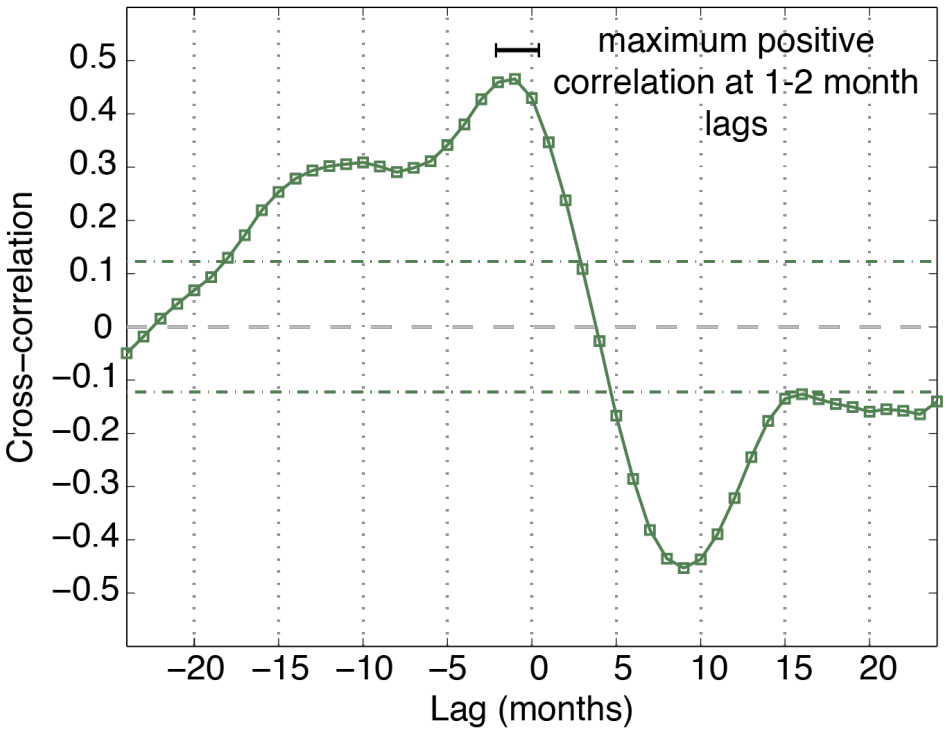

Fig. S8. Lag correlation of ONI against monthly X_{CO2} anomalies in the Niño 3.4 region. Lags less than 0 indicate a delay in the response of the X_{CO2} anomalies to the SST anomalies. The horizontal dashed green lines are based on a non-parametric test and indicate the correlation required to meet the 95% significance criteria.

Month	Year	Pressure (hPa)	sw xCO_2 (µmol mol^{-1})	air xCO_2 (µmol mol^{-1})	SST (°C)	SSS (psu)	ΔpCO_2 (µatm)
10	2014	1008.4	475.0	397.5	28.42	35.31	74.3
11	2014	1007.1	471.5	397.1	28.91	35.08	71.1
12	2014	1005.7	469.3	397.5	29.12	34.72	68.5
1	2015	1005.9	480.2	398.1	28.68	35.15	78.4
2	2015	1006.5	483.0	397.9	28.50	35.18	81.3
3	2015	1006.5	470.0	398.1	28.97	35.15	68.6
4	2015	1006.7	458.6	397.1	29.59	35.07	58.7
5	2015	1007.4	431.5	396.7	29.93	34.82	33.2
6	2015	1006.1	409.8	396.7	30.18	34.54	12.5
7	2015	1007.8	407.3	396.7	30.02	34.44	10.1
8	2015	1007.1	402.6	396.5	30.36	34.38	5.8
9	2015	1007.4	404.9	396.0	30.53	34.32	8.4
10	2015	1007.7	402.5	395.6	29.87	34.23	6.5
11	2015	1005.8	411.6	395.9	29.09	34.25	14.7
12	2015	1006.9	400.0	399.0	30.52	34.12	0.9
1	2016	1007.7	402.0	398.9	29.75	34.23	3.0
2	2016	1007.2	409.5	398.4	29.76	34.34	10.5
3	2016	1008.8	443.6	398.6	29.59	34.89	42.2
4	2016	1008.7	476.6	399.8	28.85	35.12	73.6
5	2016	1009.3	485.3	399.1	28.52	35.22	82.6

Table S1. Monthly-averaged real time data from the TAO 0°, 170°W mooring used to calculate ΔpCO_2. Monthly atmospheric pressure and seawater (sw) and air xCO_2 values are averaged from 3-hourly $MAPCO_2$ data. Monthly SST and SSS values are averaged from daily-averaged National Data Buoy Center (NDBC) TAO CTD data (from: http://tao.ndbc.noaa.gov/tao/data_download/search_map.shtml). Note that the October 2014 monthly average only includes data from 10/15/2014 - 10/31/2014; all other months include a full month of data. Surface CTD or real time data transmissions seemed to intermittently fail at this site between 11/16/2014 and 11/30/2015, and were replaced by data from the TAO 2°N, 170°W mooring (during data overlap in the time series, TAO 2°N, 170°W SST and SSS were -0.04±0.44 (1σ) and 0.16±0.18 (1σ), respectively, compared to 0°, 170°W).

Supporting References and Notes

94. D. Crisp *et al*., The orbiting carbon observatory (OCO) mission. *Trace Constituents in the Troposphere and Lower Stratosphere* **34**, 700-709 (2004).

95. R. Pollock *et al.*, The Orbiting Carbon Observatory instrument: performance of the OCO instrument and plans for the OCO-2 instrument. *Proc. SPIE* 7826, *Sensors, Systems and Next Generation Satellites – XIV* **78260W** (2010).

96. T. E. Taylor *et al.*, Orbiting Carbon Observatory-2 (OCO-2) cloud screening algorithms: validation against collocated MODIS and CALIOP data. *Atmospheric Measurement Techniques* **9**, 973–989 (2016).

97. R. Nelson *et al.*, The potential of clear-sky carbon dioxide satellite retrievals. *Atmospheric Measurement Techniques* **9**, 1671–1684 (2016).

98. C. O'Dell *et al.*, The ACOS CO_2 retrieval algorithm – Part 1: Description and validation against synthetic observations. *Atmospheric Measurement Techniques* **5**, 99-121 (2012).

99. D. Crisp *et al.*, The ACOS CO_2 retrieval algorithm--Part II: Global X_{CO2} data characterization. *Atmospheric Measurement Techniques* **5**, 687–707 (2012).

100. J. Worden *et al.*, Evaluation, Validation, And Attribution Of OCO-2 X_{CO2} Uncertainties. *Atmos. Meas. Tech. Disc*. Available at doi:10.5194/amt-2016-175, in review (2016).

101. H. Lindqvist *et al.*, Does GOSAT capture the true seasonal cycle of carbon dioxide? *Atmospheric Chemistry and Physics* **15**, 13023–13040 (2015).

102. O. Schneising *et al.*, Long-term analysis of carbon dioxide and methane column-averaged mole fractions retrieved from SCIAMACHY. *Atmospheric Chemistry and*

Physics **11**, 2863–2880 (2011).

103. J. P. F. Fortuin, H. Kelder, An ozone climatology based on ozonesonde and satellite measurements. *Journal of Geophysical Research-Atmospheres* **103**, 31709 – 31734 (1998).

104. W. J. Randel, F. Wu, A stratospheric ozone profile data set for 1979–2005: Variability, trends, and comparisons with column ozone data. *Journal of Geophysical Research-Atmospheres* **112**, D06313 (2007).

105. R. D. McPeters, G. J. Labow, Climatology 2011: An MLS and sonde derived ozone climatology for satellite retrieval algorithms. *Journal of Geophysical Research-Atmospheres* **117**, D10303 (2012).

106. H. Nguyen, N. Cressie, A. Braverman, Multivariate Spatial Data Fusion for Very Large Remote Sensing Datasets. *Remote Sensing* **9**, 142 (2017).

107. R. F. Weiss, Carbon dioxide in water and seawater: the solubility of a non-ideal gas. *Marine Chemistry* **2**, 203–215 (1974).

108. M. N. Deeter *et al.*, Operational carbon monoxide retrieval algorithm and selected results for the MOPITT instrument. *Journal of Geophysical Research-Atmospheres* **108**, 4399 (2003).

109. L. Emmons *et al.*, Validation of Measurements of Pollution in the Troposphere (MOPITT) CO retrievals with aircraft in situ profiles. *Journal of Geophysical Research-Atmospheres* **109**, 13 (2004).

110. H. M. Worden *et al.*, Decadal record of satellite carbon monoxide observations. *Atmospheric Chemistry and Physics* **13**, 837-850 (2013).

111. Y. Yin *et al.*, Decadal trends in global CO emissions as seen by MOPITT.

Atmospheric Chemistry and Physics **15**, 13433-13451 (2015).

112. M. N. Deeter *et al.*, The MOPITT Version 6 product: algorithm enhancements and validation. *Atmospheric Measurement Techniques* **7**, 3623-3632 (2014).

113. M. N. Deeter *et al*., Validation and analysis of MOPITT CO observations of the Amazon Basin. *Atmospheric Measurement Techniques* **9**, 3999-4012 (2016).

114. J. F. Lamarque *et al.*, Identification of CO plumes from MOPITT data: Application to the August 2000 Idaho-Montana forest fires. *Geophysical Research Letters* **30**, 1688 (2003).

115. A. Arellano *et al.*, Time-dependent inversion estimates of global biomass-burning CO emissions using Measurement of Pollution in the Troposphere (MOPITT) measurements. *Journal of Geophysical Research-Atmospheres* **111**, D09303 (2006).

116. Z. Jiang *et al*., Impact of model errors in convective transport on CO source estimates inferred from MOPITT CO retrievals. *Journal of Geophysical Research-Atmospheres* **118**, 2073–2083 (2013).

117. J. Worden *et al.*, El Niño, the 2006 Indonesian peat fires, and the distribution of atmospheric methane. *Geophysical Research Letters* **40**, 4938-4943 (2013).

118. R. Wanninkhof, Relationship between the wind speed and gas exchange over the ocean revisited. *Limnology and Oceanogrophy - Methods* **12**, 351-362 (2014).

119. M. G. Bosilovich *et al.*, "MERRA-2: File Specification" (Tech. Rep. Global Modeling and Assimilation Office, Office Note No. 9, 2016).

120. K. R. Gurney *et al*., TransCom 3 CO_2 inversion intercomparison: 1. Annual mean control results and sensitivity to transport and prior flux information. *Tellus Series B-Chemical and Physical Meteorology* **55**, 555-579 (2003).

121. K. R. Gurney *et al.,* Towards robust regional estimates of CO_2 sources and sinks using atmospheric transport models. *Nature* **415**, 626-630 (2002).

122. P. A. Pickers, A. C. Manning, Investigating bias in the application of curve fitting programs to atmospheric time series. *Atmospheric Measurement Techniques* **8**, 1469-1489 (2015).

123. K. W. Thoning, P. P. Tans, W. D. Komhyr, Atmospheric carbon dioxide at Mauna Loa Observatory, 2. Analysis of the NOAA/GMCC data, 1974-1985. *Journal of Geophysical Research-Atmospheres* **94**, 8549-8565 (1989).

124. W. Ebisuzaki, A Method to Estimate the Statistical Significance of a Correlation When the Data Are Serially Correlated. *Journal of Climate* **10**, 2147-2153 (1997).